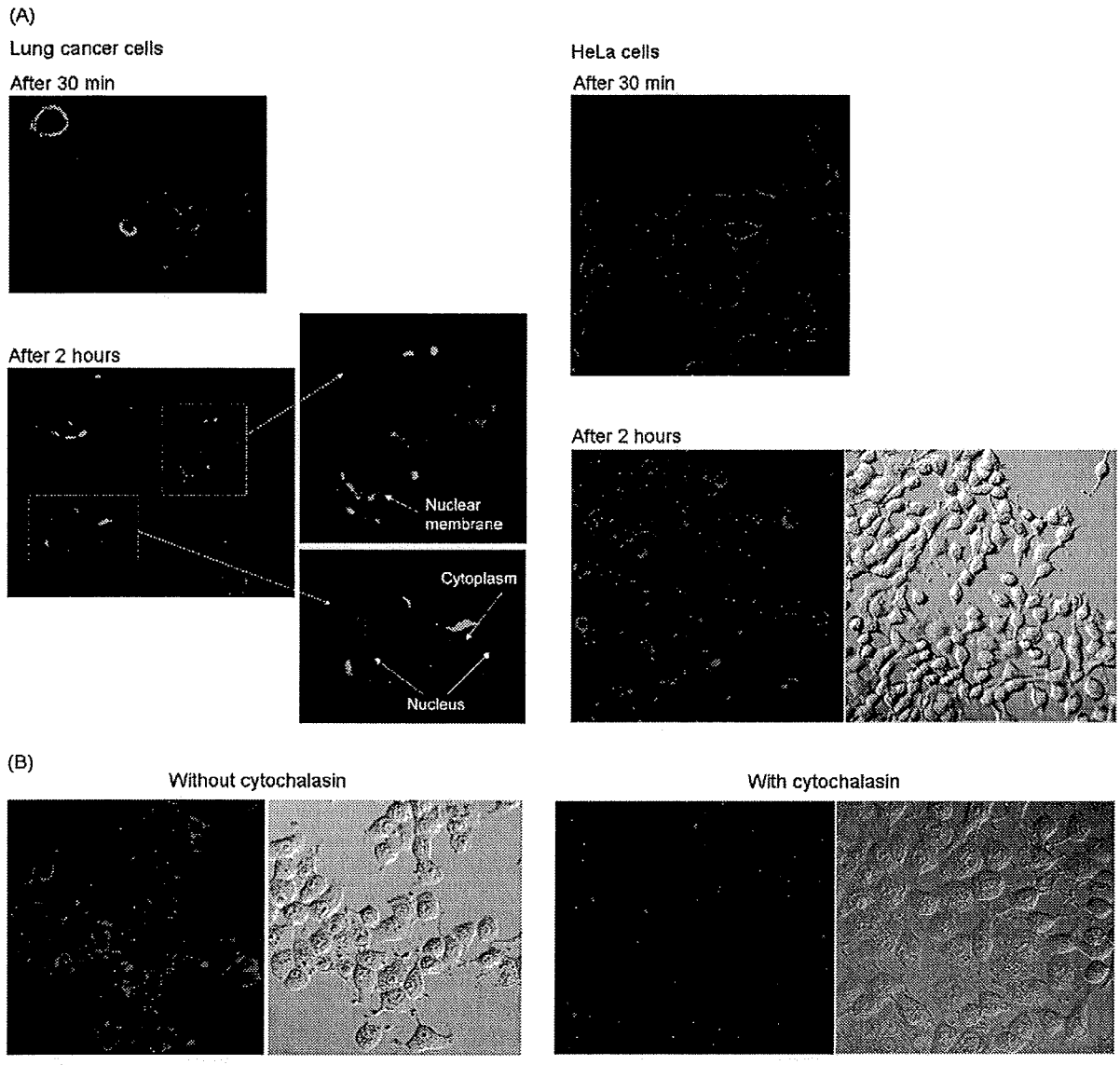


**Figure 3.** (A) Fluorescent confocal images of the intracellular delivery of multimodal silica-shelled QD probe in living cultured cells. The cells, dispensed in 96-well glass plates, were incubated with the probe (approximately 500 nM of QDs) within 30 min or 2 h in humidified atmosphere (5% $CO_2$, 37 °C), in the dark. After incubation, the cells were washed three times with PBS and subjected to fluorescent confocal microscopy. (B) Fluorescent confocal images of intracellular delivery of the QD probe in living cells in the absence and in the presence of cytochalasin (5 $\mu$g/mL). The cells were incubated with the probe within 2 h in humidified atmosphere (in the dark), washed three times with PBS, and subjected to fluorescence confocal microscopy. In both cases, the images were obtained using an Olympus FV1000 microscope (excitation wavelength, 488 nm; emission filters, 535 nm for lung cancer cells, 615 nm for HeLa cells; differential interference contrast; section scanning).

$T_1$ weighted imaging: Two dimensional (2D), multislice, $T_1$ weighted images were obtained using a conventional SE sequence with the following parameters: Pulse repetition time (TR) = 177 or 400 ms, echo time (TE) = 6.65 ms, matrix size = 64 × 64, slice orientation = horizontal, field of view (FOV) = 6.4 × 3.2 $mm^2$, slice thickness (ST) = 3 mm, and number of acquisitions (NA) = 1.

Multiecho imaging: 2D multislice multiecho imaging were performed to generate $T_2$ maps with the following parameters: TR = 6000 ms, TE = 6.65, 13.3, 19.95, 26.6, 33.25, 39.9, 46.55, 53.2, 59.85, 66.5, 73.15, 79.8, 86.45, 93.1, 99.75, and 106.4 ms, number of echoes = 16, matrix size = 64 × 64, slice orientation = horizontal, FOV = 6.4 × 3.2 $mm^2$, ST = 3 mm, and NA = 1.

Inversion–recovery: 2D multislice inversion–recovery MRIs were obtained using a spin–echo acquisition for $T_1$ map calculation with the following parameters: TR = 6000 ms, TE = 6.65 ms, inversion time = 6.45, 400, 800, 1200, 1600, 2000, 3000, 4000 ms, matrix size = 64 × 64, slice orientation = horizontal, FOV = 6.4 × 3.2 $mm^2$, ST = 3 mm, and NA = 1.

Quantitative $T_1$ maps were calculated by a nonlinear least-squares fitting using inversion–recovery MRIs. In addition, quantitative $T_2$ maps were calculated by a nonlinear least-squares fitting using multiecho imaging. All calculations and analyses were performed using *MRVision* image analysis software (version 1.5.8, MRVision Co., MA) on Solaris (Sun Microsystems, Inc., CA) and Macintosh (Mac OS X, version 10.4, Apple Computer, CA). All data are presented as mean ± SD.

**Intracellular Delivery of Multimodal QDs (Fluorescent Confocal Microscopy).** 10 $\mu$L of QD probe (50 pmol) was incubated with 90 $\mu$L cancer cells (containing 1 × $10^5$ cells) in medium, within 30 min or 2 h, in a humidified atmosphere. The cell suspension was washed twice by PBS and analyzed by fluorescence confocal microscopy for intracellular delivery

of QDs. An Olympus FV1000 microscope was used in the analysis (excitation wavelength, 488 nm; emission filters, 535 or 615 nm; differential interference contrast; section scanning).

**Photosensitization.** The cells (90 $\mu$L, 2 × $10^5$ cells/mL) were incubated with QDs (50 pmol in 10 $\mu$L) in medium,within 24 h, in humidified atmosphere (5% $CO_2$, 37 °C). The cells were washed twice with fresh medium and subjected to irradiation with laser or UV mercury lamp.

The laser irradiation of the cell suspension was carried out continuously on a confocal microscope for 30 min, changing the plane of irradiation in the well area (96-well plate). The cells were washed twice with PBS, and cell viability was detected using flow cytometry.

The UV irradiation was carried out under the experimental scheme mentioned below, to ensure irradiation with low-intensity UV light without significant heating of the sample and side effects: mercury lamp → UV-filter (UTF-34U, Sigma-Koki) (to restrict the light under 340 nm) → quartz platform → plates with cell suspension. The samples were placed in a fixed position relative to the camera to ensure equal spatial distribution of the energy during irradiation. The irradiation was carried out with the following regime: 10 min irradiation followed by 10 min break, repeated for a total duration of 30 min. Time-dependent monitoring of the level and spatial distribution of the energy during UV irradiation was carried out and was found to be relatively constant during the experiment. The temperature of the sample was also monitored over time and was found to vary in the interval 22−28 °C. After irradiation, the cells were washed twice by PBS, and the cell viability was detected by flow cytometry.

In both cases, the control samples contained QD nontreated cells.

**Cytotoxicity Test (Flow Cytometry).** The cells (2 × $10^5$ cells/mL) were incubated with QDs (500 nM; $\lambda_{em}$ = 525 nm—green fluorescence) in medium, within 24 h, in a humidified atmosphere (5% $CO_2$, 37 °C), and after that washed twice by PBS. The dead cells were labeled by propidium iodide (PI), and cell viability was analyzed by flow cytometry (flow cytometer Beckman Coulter-Epics XL). The flow cytometer was operated in accordance with the manufacturer's recommendations after fine adjustments for optimization. The forward- and site-scatter parameters were adjusted to accommodate the inclusion of both live and dead cells within the acquisition data with quadrant markers drawn to distinguish PI labeled dead cells (red fluorescence) from PI nonlabeled viable cells. The control sample contained QD nontreated cells. The viability of QD treated cells was calculated as the percentage from viability of nontreated (control) cells. No cells were excluded from the analysis and ~5000 cells were counted for each sample. The data were collected and analyzed using *XL System II* software.

**Pharmacodynamics.** Mice (ICR, ~20−25 g) were injected intravenously through the tail vain with 50 pmol (in 100 $\mu$L, a single injection) multimodal silica-shelled QDs. Serial sacrifices were carried out at the sixth and 24th hour after the injection. Several organs (brain, spleen, liver, lung, kidneys) were isolated, homogenized, and analyzed for QD amount, using NMR spectroscopy.

**Two-Photon Imaging of Brain Circulation *in Vivo*.** The animal (Sprague−Dawley rats, $n$ = 4, ~340 g) was anesthetized with isoflurane (4% for induction, 2% for surgery, and 1.4% during the measurements). The tracheal intubation was performed, and the femoral vein was catheterized for drug administration. The skull over the somatosensory cortex (3 mm × 3 mm) was removed, and the dura was kept intact. The body temperature was maintained (37 °C), and the systemic arterial blood pressure was periodically monitored from the tail artery. The heartbeat and end tidal gas levels were continuously monitored. To visualize brain microcirculation, 5% FITC−Dextran (70 kDa) was intravenously (i.v.) injected (0.3 mL/h), and excited with 900 nm pulse-laser (Maitai HP, Spectral Physics) under a microscope (SP5, Leica) equipped with a 10× objective lens (0.30 numerical aperture). The vessel diameter was then determined by measuring the width of the vessel image projected across the 15 $z$-images (up to ~0.3 mm from the cortical surface) in each vessel segment. All measured parameters were considered as controls under the conditions mentioned above. After the stoppage of FITC−Dextran infusion, FITC−Dextran was partially washed from the brain circulation by short i.v. infusion of saline solution. Then, QD was injected (single injection, 0.3 mL of 0.5 $\mu$M QD concentration) into the rat, and all parameters were measured as described above.

## RESULTS AND DISCUSSION

**Structure and Characterization of Multimodal Silica-Shelled QDs.** Our multimodal QD probe was composed of single QD micelles incorporated in small silica spheres (15−20 nm in diameter) and amphiphilic gadolinium complex [tris(2,2,6,6-tetramethyl-3,5-heptanedionate)/gadolinium, trivial name Resolve Al−Gd] incorporated into the micelle part and/or silica coat (Figure 1A). For comparison, we used a second probe, consisting of QDs conjugated with DOTA-Bn-NCS/gadolinium (Figure 1B).

In the first probe, the micelle around the QD allows an incorporation of strongly hydrophobic paramagnetic substances in the silica sphere. The hydrophobic micelle isolates QD nanocrystal from the polar molecules, penetrating from the environment in the silica sphere, and maintains the fluorescent properties. At the same time, the paramagnetic molecules, incorporated in the silica coat or micelle, are accessible to the water, which is beneficial for $^1$H MRI contrast agents and, in particular, for gadolinium ions. The surface of the silica sphere was amino-functionalized and ready for bioconjugation. At acidic pH (3.0), the probe (A) had a surface potential of +31 mV (detected by zeta-potential titration), which decreased to −37 mV at pH 10.0. At physiological pH (7.4), the zeta potential was +6.9 mV.

Both probes consist of a single QD per one silica sphere (Figure 2A), which allows normalization of their concentrations to the QD concentration in moles and facilitates the dose-dependent analyses in life science research. Both probes strongly retain about 25−30% of the gadolinium complex added initially to the reaction mixture (Figure 2B). The concentration of the gadolinium complex decreased during purification by dialysis up to 10 h. After this time, there were no changes (Figure 2B), which was an indication for a retention of the complex in the silica coat or on the surface of the silica sphere.

The close distance between QDs and paramagnetic substances (especially paramagnetic nanoparticles) results in a decrease of their fluorescent and paramagnetic characteristics in comparison with the isolated materials (*13, 15*). In the present study, we compared the spectral properties of both multimodal probes, described above (Figure 2C). In probe A, gadolinium ions are in close proximity to QD (Figure 1A), and in probe B, gadolinium ions are far from QD (Figure 1B). The fluorescence quantum yield (QY) of both probes was ~35−50% in aqueous solution (depending on QD size). It was ~1.4 times lower than the QY of QDs in organic solvent and the same as the QY of silica-shelled QDs without gadolinium. The incorporation of gadolinium ions into the silica sphere also did not affect the profile of the absorbance and fluorescent spectra of silica-shelled QDs, as well as their paramagnetic characteristics. After purification, $T_1$ (longitudinal relaxation time) and $T_2$ (transverse relaxation time) of probe (A) were shorter than $T_1$ and $T_2$ of probe (B) (Figure 2C). We calculated that the numbers of

(A) $T_1$ weighted images

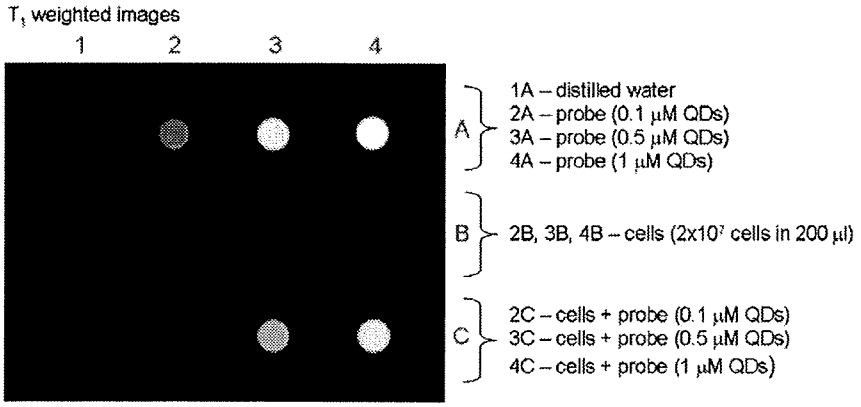


$T_1$ quantitative (ms)

| | 2 | 3 | 4 |
|---|---|---|---|
| A (probe) | 606.7 +/- 5.5 | 220.9 +/- 1.9 | 114.8 +/- 1.5 |
| C (probe + cells) | 1243.6 +/- 9.3 | 358.8 +/- 4.9 | 186.6 +/- 1.7 |

Distilled water: $T_1$ = 3030.9 +/- 20.6 ms. Cells only: $T_1$ = 3017.6 +/- 26.3 ms.

(B) $T_2$ weighted images

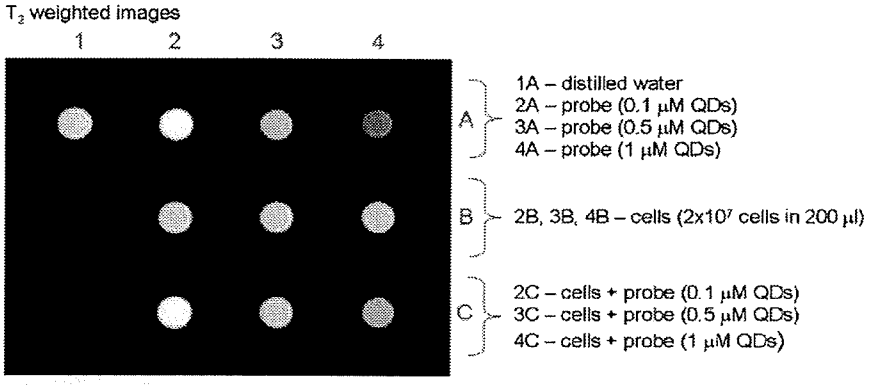


$T_2$ quantitative (ms)

| | 2 | 3 | 4 |
|---|---|---|---|
| A (probe) | 261.8 +/- 3.3 | 138.0 +/- 1.6 | 81.3 +/- 0.8 |
| C (probe + cells) | 304.7 +/- 3.3 | 176.8 +/- 1.9 | 114.9 +/- 1.0 |

Distilled water: $T_2$ = 440.0 +/- 9.4 ms. Cells only: $T_2$ = 368.0 +/- 7.0 ms.

**Figure 4.** $T_1$- and $T_2$-weighted images and quantitative values of samples, containing probe only (A2−A4), cells only (B2−B4), or cells incubated with probe (C2−C4). Incubation conditions: Lung cancer cells ($2 \times 10^7$) were dispensed in plates, containing 20 mL cultured medium. The probe was added to the plates in different concentrations (1 $\mu$M, 0.5 $\mu$M, or 0.1 $\mu$M QDs, respectively). The incubation was carried out during 2 h in humidified atmosphere (5% $CO_2$, 37 °C). The cells were collected by centrifugation, washed three times by PBS (containing 1% Trypsin), and finally resuspended in 200 $\mu$L PBS. All samples were treated in the same manner. The concentration of the probe in moles was approximate. It was calculated from the absorbance spectra of QD incorporated into the silica spheres, using the equation of Yu et al. (*38*). The MRI measurements were performed in a 7.0 T magnet (Kobelco, Japan) interfaced to a Bruker Avance console (Bruker Medical GmbH, Germany). A 70 mm diameter volume coil (Bruker) was used for measurement of the samples. The sample temperature was maintained at room temperature (~22−24 °C). The measurements were performed as follows: $T_1$-weighted imaging using conventional spin−echo (SE) sequence and inversion−recovery SE imaging for $T_1$ calculations. The multiecho SE imaging was measured for $T_2$-weighted imaging and $T_2$ calculations.

chelating molecules attached on or incorporated in one silica sphere were approximately same (Gd/QD ~ 18:1 and ~17.6:1, mol/mol, for probe A and probe B, respectively). This indicates that the incorporation of gadolinium in close proximity to QD

**Table 1. Cytotoxicity and Photosensitization of Multimodal Silica-Shelled QDs**

| treatment | HeLa cells[a] | A549 cells[a] | Jurkat cells[a] | K562 cells[a] |
|---|---|---|---|---|
| + 500 nM QDs | 98 +/− 6 | 95 +/− 9 | 97 +/− 7 | 101 +/− 5 |
| + Laser irradiation | 96 +/− 8 | 97 +/− 9 | 98 +/− 5 | 98 +/− 8 |
| + 500 nM QDs + Laser irradiation | 95 +/− 4 | 98 +/− 10 | 96 +/− 6 | 96 +/− 8 |
| + UV irradiation | 87 +/− 4 | 89 +/− 5 | 91 +/− 5 | 89 +/− 6 |
| + 500 nM QDs + UV irradiation | 85 +/− 7 | 84 +/− 8 | 88 +/− 3 | 87 +/− 6 |

[a] Cell viability (% from control). The control samples contain nontreated cells. The results are mean +/− SD from four independent experiments.

does not significantly affect its paramagnetic properties, presumably because of the isolation of both materials from the hydrophobic micelle.

All experiments on viable cells and animals were performed using probe A only.

**Direct Intracellular Delivery of Multimodal Silica-Shelled QDs.** Figure 3A represents fluorescent images of HeLa and lung cancer cells, labeled with probe A. The amino-functionalized (and positively charged) probe possessed an easy and comparatively fast intracellular delivery without transfection techniques. It was found that the probe penetrates through the cytoplasmic membrane via an endocytotic mechanism. The cytochalasin (an inhibitor of endocytosis) suppressed its intracellular delivery (Figure 3B). The probe was localized into the cytoplasm, uniformly distributed. A concentration of the probe in close proximity to the nuclear membrane was detected, which indicates an interaction with some intracellular compartments. No fluorescence was detected in the nucleus within 4 h incubation.

The facilitated permeability of silica-shelled QDs allows their application in the detection of intracellular targets (antigens, membrane compartments, subcellular organelles, etc.) in viable cells without transfection techniques. Currently, QDs are applied predominantly for labeling of cell surface antigens *in vitro* and *in vivo* or for extra- and intracellular labeling of fixed cells. Their application for labeling of intracellular components in viable cells requires transfection techniques for penetration through plasmatic membrane. The already published data indicate that QDs could be delivered in viable mammalian cells via four different mechanisms: nonspecific endocytosis/pinocytosis facilitated by polycationic transfectants (as lipofectamine); microinjection; electroporation; and peptide-induced transport (*24*−*28*). It is widely accepted that the transfection techniques maintain the risk of artifacts, some of them are toxic, and they have to be replaced with direct approaches for intracellular delivery of QDs. We observed that an appropriate polymer coating of QDs (such as positively charged silica) could facilitate their direct intracellular delivery and random distribution into the cells (*29*), which was also reported by other authors (*30*).

If the cells were washed several times with phosphate-buffered saline, concentrated, and subjected to MRI, a high MRI contrast was observed on the $T_1$- and $T_2$-weighted images (Figures 4). The $T_1$ and $T_2$ values allow calculation of the approximated absolute amount of multimodal QDs delivered into the cells, using two independent calibration curves. The calibration curve represents the relationship between the pure probe in known concentrations and $T_1$ or $T_2$ values, respectively. It was found that approximately 58−75% of the probe was delivered into the cells and/or bound on the cell surface.

**Cytotoxicity, Photosensitization, and Pharmacodynamics.** All experiments with cultured cells were provided in medium without FBS. The cell viability of A459, Jurkat, K562, and HeLa cells was ~100% after 24 h incubation with QDs in 500 nM concentration (Table 1). The nanoparticles (500 nM) were also nontoxic under continuous UV or laser irradiation of the cell suspension after preliminary incubation with QDs for 24 h. The cell viability did not change within 30 min of continuous laser irradiation of QD-treated and QD-nontreated (control) cells. Under UV irradiation, the viability of QD-treated and QD-nontreated (control) cells decreased slightly (~10%) in comparison with nonirradiated cells, as a result of nonspecific effects of UV light on cell viability (Table 1).

Several groups have demonstrated photosensitization of living cells using CdSe or CdTe core QDs (*31*−*35*). However, the overcoating (inorganic or organic) usually suppresses or eliminates the photosensitization effect (*31, 32, 35*).

Regarding cytotoxicity of nanoparticles, it is necessary to note that this parameter is usually clarified on cancer cells that are inherently resistant to many external agents. The data on normal cells are scanty. Currently, there are insufficient data on the metabolism of QDs in live organisms, and it is not clear what will happen if the nanoparticles are accumulated in different organs for a long time. Their excretion through kidneys avoiding any long-term accumulation and metabolism in the liver, bone marrow, or other organs seems to be the best possibility. Choi and colleagues have demonstrated that a hydrodynamic diameter of <5.5 nm of organic-coated QDs results in rapid and efficient renal filtration and urinary excretion from the body. Increasing the diameter by >15 nm usually prevents renal excretion and increases the blood half-life by about 300 times and the whole body half-life by about 700 times (*36*). The authors also have reported that the purely cationic charge is associated with an increase in hydrodynamic diameter of the QDs after incubation with serum.

Our pharmacodynamic study shows that nonPEGylated silica-shelled QDs persist in the blood circulation within an hour after i.v. injection in mice (half-life ~20 min). Six hours after the injection, a comparatively large amount of QDs were detected in spleen, a very low amount in liver and kidney, and none in lung and brain (data are not shown). A similar result was obtained 24 h after the injection. Recently, Yang and colleagues reported that QDs (commercial Qtracker 705) are accumulated predominantly in spleen, liver, and kidney after i.v. injection in mice, and they do not metabolize within 28 h (*36*).

**Effects on Physiological Characteristics and Brain Circulation.** The intravenous application of the probe in rat did not affect significantly the physiological parameters, e.g., hart rate, blood pressure, and microcirculation (Figure 5). The multimodal QDs (300 $\mu$L of 1 $\mu$M stock solution) were injected into the femoral vain. Ten minutes after the injection, the heart rate increased slightly with subsequent normalization to the baseline level within 40 min. The blood pressure was stable within 20 min after the injection and decreased about 10% after 80 min (Table 2). The brain vasculature was visualized in the somatosensory cortex using two-photon microscopy, and the fluorescence was detected up to a 200 $\mu$m depth (Figure 5). The probe did not affect the diameter and structure of the blood vessels, which makes it an appropriate tracer for brain vasculature in the study of brain phenomena, e.g., visualization of neuron/astrocyte/blood vessel structure and investigation of neurovascular coupling.

In conclusion, the described strategy of the design of multimodal QDs allows the development of probes with high fluorescent and paramagnetic contrast characteristics and comparatively soft effects on cell homeostasis and animal physiology. The described QD probe is appropriate for *in vitro* and *in vivo* tracing of cells and blood vessels, simultaneously using fluorescent microscopy and MRI. After conjugation with appropriate ligands, the probe could be applied for target-selective molecular imaging *in vitro* and *in vivo*. The easy intracellular


**Figure 5.** Two-photon images of brain circulation before and after i.v. injection of multimodal silica-shelled QDs in rat. In the images: (A) FITC−Dextran (0.5 mL of 5 $\mu$M concentration) was injected in ~340 g rat, and the image was obtained after 20 min at $\lambda_{ex}$ = 900 nm and $\lambda_{em}$ = 525 nm. (B) FITC−Dextran was washed from the brain vasculature by i.v. infusion of saline solution, and the image was obtained at $\lambda_{ex}$ = 900 nm and $\lambda_{em}$ = 525 nm. (C) QDs (0.3 mL of 1 $\mu$M QD concentration) were injected in the same rat. The image was obtained after 20 min at $\lambda_{ex}$ = 900 nm and $\lambda_{em}$ = 560 nm. Representative images from three independent experiments are shown in the figure.

**Table 2. Physiological Characteristics before and After i.v. Injection of Silica-Shelled QDs in Experimental Animals under Anesthesia**[a]

| parameter | before | ~20 min after i.v. injection |
|---|---|---|
| blood pressure, (mmHg) | 95.3 +/− 7.8 | 93.5 +/− 16.2 |
| heart rate, (BPM) | 304 +/− 62 | 348 +/− 43 |
| blood vessel diameter | | |
| arteries, ($\mu$m) | 26 +/− 8 | constant |
| veins, ($\mu$m) | 43 +/− 20 | constant |

[a] $n$ = 3 ($n$ = number of rats in the group); QD concentration = 80 pmol (in 300 L).

delivery of these silica-shelled QDs allows avoidance of conventional transfectants that are inherently toxic.

## ACKNOWLEDGMENT

The technical assistance of Misao Yoneyama and Jeff Kershaw (NIRS, Chiba, Japan) in MRI measurements and data analysis is gratefully acknowledged. The animal experiments were approved by the Animal Care and Use Committee of NIRS-Chiba.

## LITERATURE CITED

(1) Alivisatos, A. P., Gu, W., and Larabell, C. Quantum dots as cellular probes. *Annu. Rev. Biomed. Eng. 7*, 55–76.

(2) Redl, F. X., Cho, K.-S., Murray, C. B., and O'Brien, S. (2003) Three-dimensional binary superlattices of magnetic nanocrystals and semiconductor quantum dots. *Nature 423*, 968–971.

(3) Wang, D. S., He, J. B., Rosenzweig, N., and Rosenzweig, Z. (2004) Superparamagnetic $Fe_2O_3$ Beads-CdSe/ZnS quantum dots core-shell nanocomposite particles for cell separation. *Nano Lett. 4*, 409–413.

(4) Gu, H., Zheng, R., Zhang, X., and Xu, B. (2004) Facile one-pot synthesis of bifunctional heterodimers of nanoparticles: a conjugate of quantum dot and magnetic nanoparticles. *J. Am. Chem. Soc. 126*, 5664–5665.

(5) Michalet, X., Pinaud, F. F., Bentolila, L. A., Tsay, J. M., Doose, S., Li, J. J., Sundaresan, G., Wu, A. M., Gambhir, S. S., and Weiss, S. (2005) Quantum dots for live cells, in vivo imaging, and diagnostics. *Science 307*, 538–544.

(6) Santra, S., Yang, H., Holloway, P. H., Stanley, J. T., and Mericle, R. A. (2005) Synthesis of water-dispersible fluorescent, radio-opaque, and paramagnetic CdS:Mn/ZnS quantum dots: a multifunctional probe for bioimaging. *J. Am. Chem. Soc. 127*, 1656–1657.

(7) Yi, D. K., Selvan, S. T., Lee, S. S., Papaefthymiou, G. C., Kundaliya, D., and Ying, J. Y. (2005) Silica-coated nanocomposites of magnetic nanoparticles and quantum dots. *J. Am. Chem. Soc. 127*, 4990–4991.

(8) Know, K.-W., and Shim, M. (2005) $\gamma$-$Fe_2O_3$/II-VI sulfide nanocrystal heterojunctions. *J. Am. Chem. Soc. 127*, 10269–10275.

(9) Pellegrino, T., Kudera, S., Liedl, T., Javier, A. M., Manna, L., and Parak, W. J. (2005) On the development of colloidal nanoparticles towards multifunctional structures and their possible use for biological applications. *Small 1*, 48–63.

(10) Kim, H., Achermann, M., Balet, L. P., Hollingsworth, J. A., and Klimov, V. I. (2005) Synthesis and characterization of Co/CdSe core/shell nanocomposites: bifunctional magnetic-optical nanocrystals. *J. Am. Chem. Soc. 127*, 544–546.

(11) Know, K.-W., Lee, B. H., and Shim, M. (2006) Structural evolution in metal oxide/semiconductor colloidal nanocrystal heterostructures. *Chem. Mater. 18*, 6357–6363.

(12) Pellegrino, T., Fiore, A., Carlino, E., Giannini, C., Cozzoli, P. D., Ciccarella, G., Respaud, M., Palmirotta, L., Cingolani, R., and Manna, L. (2006) Heterodimers based on CoPt3-Au nanocrystals with tunable domain size. *J. Am. Chem. Soc. 128*, 6680–6698.

(13) Cozzoli, P. D., Pellegrino, T., and Manna, L. (2006) Synthesis, properties and perspectives of hybrid nanocrystal structures. *Chem. Soc. Rev. 35*, 1195–1208.

(14) Mulder, W. J. M., Koole, R., Brandwijk, R. J., Storm, G., Chin, P. T. K., Strijkers, G. J., Donega, C. M., Nicolay, K., and Griffioen, A. W. (2006) Quantum dots with a paramagnetic coating as a bimodal molecular imaging probe. *Nano Lett. 6*, 1–6.

(15) Selvan, S. T., Patra, P. K., Ang, C. Y., and Ying, J. Y. (2007) Synthesis of silica-coated semiconductor and magnetic quantum dots and their use in the imaging of live cells. *Angew. Chem., Int. Ed. 46*, 1–6.

(16) Wang, S., Jarrett, B. R., Kauzlarich, S. M., and Louie, A. Y. (2007) Core/shell quantum dots with high relaxivity and photoluminescence for multimodality imaging. *J. Am. Chem. Soc. 129*, 3848–3856.

(17) Prinzen, L., Miserus, R.-J., Dirksen, A., Hackeng, T. M., Deckers, N., Bitsch, N. J., Megens, R. T. A., Douma, K., Heemskerk, J. W., Kooi, E., Frederik, P. M., Slaaf, D. W., Zandvoort, M., and Reutelingsperger, C. P. M. (2007) Optical and magnetic resonance imaging of cell death and platelet activation using annexin a5-functionalized quantum dots. *Nano Lett. 7*, 93–100.

(18) Oostendorp, M., Douma, K., Stelt, B. J., Hackeng, T. M., Dirksen, A., Van Zandvoort, M. A., Post, M. J., and Backes, W. H. (2007) Feasibility of cNGR labeled paramagnetic quantum dots for molecular MRI and two-photon laser scanning microscopy of neovascularization. *Proc. Int. Soc. Magn. Reson. Med. 15*, 1164.

(19) Grant, S. C., Zheng, T., Marshall, G. P., Yang, H., Dutta, D., Cornnell, H., Santra, S., Holloway, P. H., Moudgil, B. M., Scott, E. W., Laywell, E. D., Walter, G. A., Edison, A. S., Steindler, D. A., and Weiss, M. D. (2006) MR microscopy of multipotent

astrocytic stem cells labeled with multimodal QDots applied to a neonatal murine model of hypoxic ischemic encephalopathy. *Proc. Int. Soc. Magn. Reson. Med. 14*, 1990.

(20) Bakalova, R., Zhelev, Z., Aoki, I., and Kanno, I. (2007) Designing quantum dot probes. *Nat. Photonics 1*, 487–489.

(21) Bakalova, R., Zhelev, Z., Aoki, I., Ohba, H., Imai, Y., and Kanno, I. (2006) Silica-shelled single quantum dot micelles as imaging probes with dual or multimodality. *Anal. Chem. 78*, 5925–5932.

(22) Bryant, L. H., Brechbiel, M. W., Wu, C., Bulte, J. W. M., Herynek, V., and Frank, J. A. (1999) Synthesis and relaxometry of high-generation ($G$=5, 7, 9, and 10) PAMAM dendrimer-DOTA-gadolinium chelates. *J. Magn. Res. Imaging 9*, 348–352.

(23) Wu, C., Brechbiel, M. W., Kozak, E. W., and Gansow, O. A. (1994) Metal-chelate-dendrimer-antibody constructs for use in radioimmunotherapy and imaging. *Bioorg. Med. Chem. Lett. 4*, 449–454.

(24) Dubertret, B., Skourides, P., Norris, D. J., Noireaux, V., and Libchaber, A. (2002) In vivo imaging of quantum dots encapsulated in phospholipids micelles. *Science 298*, 1759–1762.

(25) Matteakis, L. C., Dias, J. M., Choi, Y. J., Gong, J., Bruches, M. P., Liu, J., and Wang, E. (2004) Optical coding of mammalian cells using semiconductor quantum dots. *Anal. Biochem. 327*, 200–208.

(26) Jaiswal, J. K., Mattoussi, H., Mauro, J. M., and Simon, S. M. (2003) Long-term multiple color imaging of live cells using quantum dot bioconjugates. *Nat. Biotechnol. 21*, 47–51.

(27) Chen, F., and Gerion, D. (2004) CdSe/ZnS nanocrystal-peptide conjugates for long-term, nontoxic imaging and nuclear targeting in living cells. *Nano Lett. 4*, 1827–1832.

(28) Derfus, A. M., Chan, W. C. W., and Bhatia, S. N. (2004) Intracellular delivery of quantum dots for live cell labeling and organelle tracking. *Adv. Mater. 16*, 961–966.

(29) Zhelev, Z., Ohba, H., and Bakalova, R. (2006) Single quantum dot-micelles coated with silica shell as potentially non-cytotoxic fluorescent cell tracers. *J. Am. Chem. Soc. 128*, 6324–6325.

(30) Duan, H., and Nie, S. (2007) Cell-penetrating quantum dots based on multivalent and endosome-disrupting surface coatings. *J. Am. Chem. Soc. 129*, 3333–3338.

(31) Defrus, A. M., Chan, W. C. W., and Bhatia, S. N. (2004) Probing the cytotoxicity of quantum dots. *Nano Lett. 4*, 11–18.

(32) Bakalova, R., Ohba, H., Zhelev, Z., Nagase, T., Jose, R., Ishikawa, M., and Baba, Y. (2004) Quantum dot anti-CD conjugates: Are they potential photosensitizers or potentiators of classical photosensitizing agents in photodynamic therapy of cancer? *Nano Lett. 4*, 1567–1573.

(33) Bakalova, R., Ohba, H., Zhelev, Z., Ishikawa, M., and Baba, Y. (2004) Quantum dots as photosensitizers? *Nat. Biotechnol. 22*, 1361–1362.

(34) Cho, S. J., Maysinger, D., Jain, M., Roder, B., Hackbarth, S., and Winnik, F. M. (2007) Long-term exposure to CdTe quantum dots causes functional impairments in live cells. *Langmuir 23*, 1974–1980.

(35) Hardman, R. (2006) A toxicologic review of quantum dots: toxicity depends on physicochemical and environmental factors. *Environ. Health Perspect. 114*, 165–172.

(36) Choi, H. S., Liu, W., Misra, P., Tanaka, E., Zimmer, J. P., Ipe, B. I., Bawendi, M. G., and Frangioni, J. V. (2007) Renal clearance of quantum dots. *Nat. Biotechnol. 25*, 1165–1170.

(37) Yang, R. S. H., Chang, L. W., Wu, J.-P., Tsai, M.-H., Wang, H.-J., Kuo, Y.-C., yeh, T.-K., Yang, C. S., and Lin, P. (2007) Persistent tissue kinetics and redistribution of nanoparticles, quantum dot 705, in mice: ICP-MS quantitative assessment. *Environ. Health Perspect. 115*, 1339–1343.

(38) Yu, W. W., Qu, L., Guo, W., and Peng, X. (2003) Experimental determination of the extinction coefficient of CdTe, CdSe, and CdS nanocrystals. *Chem. Mater. 15*, 2854–2860.

BC700431C

# Nitroxyl radicals as low toxic spin-labels for non-invasive magnetic resonance imaging of blood–brain barrier permeability for conventional therapeutics†

Zhivko Zhelev,[a] Rumiana Bakalova,*[a] Ichio Aoki,[a] Ken-ichiro Matsumoto,[b] Veselina Gadjeva,[c] Kazunori Anzai[b] and Iwao Kanno[a]

*Received (in Cambridge, UK) 26th September 2008, Accepted 20th October 2008*
*First published as an Advance Article on the web 13th November 2008*
DOI: 10.1039/b816878d

**The present study describes a novel non-radioactive methodology for *in vivo* non-invasive, real-time imaging of blood–brain barrier (BBB) permeability for conventional drugs, using nitroxyl radicals as spin-labels and magnetic resonance imaging (MRI).**

The non-invasive real-time imaging of blood–brain barrier (BBB) permeability for drugs is an indispensible step in the preclinical and clinical testing of new pharmaceuticals for brain diseases. The precise mapping of a drug in the brain has a significant impact on its dosing and prognostication of its target-specific effect.

The conventional methods for investigation of BBB permeability are usually invasive, time- and cost-consuming, often suffer from artefacts, and require a large number of experimental animals.[1–6] *In vitro* models of BBB (*e.g.*, cell and tissue cultures, immobilized artificial membranes, *etc.*) often serve as a major approach for indirect evaluation of drug permeability for brain tissue. The development of new methodologies for *in vivo* imaging of BBB permeability which are non-invasive, environmentally friendly, with minimal animal loss and minimal risk for volunteers, is a major goal of the modern pharmaceutical industry.

Currently, radiopharmaceuticals combined with autoradiography or positron-emission tomography (PET) are the only option for non-invasive real-time imaging of BBB permeability.[7–9] Despite this approach being highly sensitive and valuable, it suffers from several restrictions which prevent it from being widely applicable in preclinical and clinical trials of new pharmaceuticals. Radio-labelling carries a risk for human safety and requires special experimental equipment and facilities, which increases markedly the cost of this analysis. Radiotracers are usually used for labelling of diagnostic markers, but not for labelling of therapeutics and real-time imaging of their BBB permeability and distribution in the organism.

[a] *Department of Biophysics, Molecular Imaging Center, National Institute of Radiological Sciences (NIRS), 4-9-1 Anagawa, Inage-ku, Chiba 263-8555, Japan. E-mail: bakalova@nirs.go.jp. E-mail: ra_bakalova@yahoo.com; Fax: +81-43-206-3276; Tel: +81-43-206-4067*
[b] *Center for Heavy-ion Particle Therapy, National Institute of Radiological Sciences (NIRS), 4-9-1 Anagawa, Inage-ku, Chiba 263-8555, Japan*
[c] *Department of Chemistry and Biochemistry, Trakia University, Stara Zagora, Bulgaria*
† Electronic supplementary information (ESI) available: Experimental details. See DOI: 10.1039/b816878d

In the present study, we would like to introduce a novel non-radioactive and environmentally friendly alternative for non-invasive real-time imaging of BBB permeability for conventional drugs, using stable nitroxyl radicals as spin-labels and magnetic resonance imaging (MRI).

Nitroxyl radicals are well known from electron paramagnetic resonance (EPR) studies.[10–13] In 1984, it was reported that they have $T_1$ contrast properties and could be applied in MRI.[14] The nitroxyls are small molecules, sensitive to the redox status of biological samples and their use in life science research is limited predominantly to tissue oxygen and redox mapping *in vitro* and *in vivo*.[10–13,15–17] The paramagnetic nitroxyl radical could be reduced to diamagnetic hydroxylamine with the loss of the EPR signal or $^1$H-MRI relaxation time and thus could serve as a reduction sensor. However, the diamagnetic hydroxylamine could be re-converted *via* oxygenation to paramagnetic nitroxyl radical with the appearance of the EPR or MRI signal and thus could serve as an oxidation sensor. The rate constants of both processes could be used for evaluation of reduction/oxidation balance in cells and tissues.

Nitroxyl radicals are characterized by comparatively high $T_1$ contrast properties, lower toxicity in comparison with the conventional MRI contrast agents (*e.g.*, gadolinium derivatives), and some of them possess an excellent cell permeability. All these characteristics make them attractive for MRI diagnostics and their application in life science research could be extended beyond the limits mentioned above. In this context, we supposed that nitroxyl radicals could be appropriate spin-labels for non-invasive real-time MRI of BBB permeability for conventional therapeutics, which is an important step in their preclinical testing. Below, we would like to give a proof of the reality of this concept. In addition, MRI is characterized by much higher spatial resolution than EPR imaging (and even PET) and gives an excellent anatomical reference, which facilitates the exact localization of a nitroxyl probe in the organism.

We synthesized a TEMPO-labelled analogue (SLENU) of the conventional anticancer drug Lomustine [1-(2-chloroethyl)-3-cyclohexyl-1-nitrosourea, CCNU] (Fig. 1). Lomustine significantly improves the health-related quality of life of patients treated for brain and other tumours.[18] Both TEMPO radical and Lomustine are permeable for BBB and cell membranes.[15,19]

Formally, the Lumustine molecule can be separated into two parts (Fig. 1). The nitrosourea ensures the anticancer

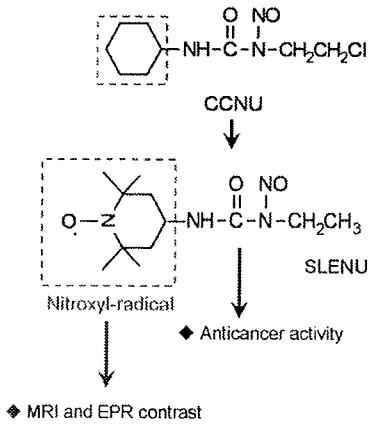


**Fig. 1** Lomustine (CCNU) and its nitroxyl labelled analogue (SLENU).

effect and could not be modified. We exchanged the cyclohexyl part of the molecule with TEMPO radical. This substitution did not influence the anticancer effect of the drug or its toxicological characteristics (*e.g.*, $LD_{50}$).[21,22] SLENU was synthesized, purified and characterized as described previously.[20] The present study was designed to clarify: (i) whether the TEMPO-labelling of nitrosourea will affect its BBB permeability and localization in the brain tissue; and (ii) whether nitroxyl radicals are appropriate spin-labels of conventional drugs for *in vivo* dynamic MR imaging of their BBB permeability.

The first step was to ensure that the TEMPO–nitrosourea bond was stable and that there was no dissociation between the two compounds in the blood. Thus, the detection of MRI signal enhancement of the nitroxyl radical could indicate the localization of nitrosourea in the brain tissue *in vivo*. In buffer, the EPR spectra of TEMPO and SLENU were distinguished by the third line in the triplet, which was shorter for SLENU (Fig. 2A). In blood, the difference between the amplitudes of line 3 became larger, however, both spectra (of TEMPO and SLENU) had the same profiles. The lower amplitude of line 3 in the EPR spectrum of SLENU could be explained by the limited motion of the conjugated nitroxyl radical (in SLENU), in comparison with free TEMPO radical. No changes in the shape of the EPR spectrum of SLENU were detected during long-term incubation in blood (Fig. 2B). This indicated that there was no dissociation of the TEMPO–nitrosourea covalent bond.

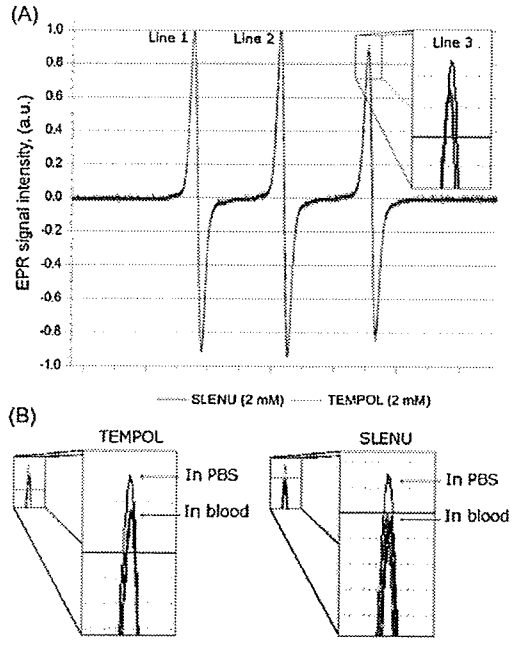


**Fig. 2** (A) Normalized EPR spectra of SLENU and TEMPOL in PBS. In blood, the EPR spectra of both substances have the same profile. (B) Amplitudes of Line 3 during long-term incubation of TEMPOL or SLENU in freshly isolated blood. For comparison, the amplitude of Line 3 in PBS is shown.

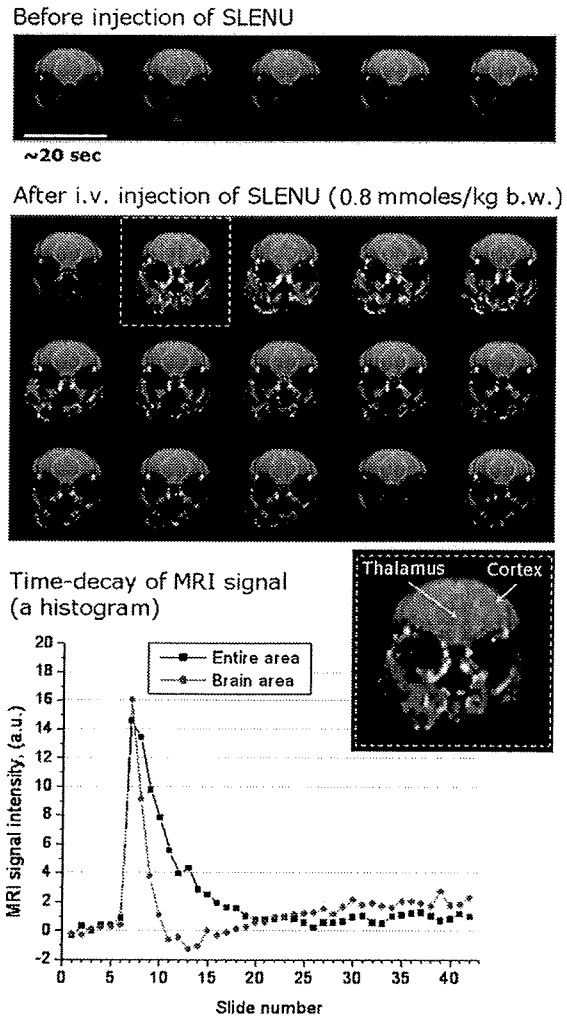


**Fig. 3** MRI signal dynamic of SLENU in the brain after intravenous injection in mice. Each image was obtained within a 20-s interval, using Gradient-echo $T_1$-weighted MRI. In the image, the red colour represents an extraction of the signal between every single slide and the averaged baseline signal (first five slides – before injection). In the chart, the red and black colours represent an MRI signal dynamic in the brain or entire area, respectively.

SLENU was injected intravenously in healthy mice *via* the tail vein and $^{1}$H-MR imaging of the brain was performed on a 7.0 Tesla horizontal MRI instrument (Fig. 3). The injected dose was below the toxic limit. The MRI-signal dynamic of SLENU (Fig. 3) in the brain and surrounding tissues followed almost the same kinetics and distribution as non-modified TEMPO radical (Fig. 1S, *Supplementary Information*†). SLENU was rapidly transported and randomly distributed into the brain tissue. Obviously, the exchange of the cyclohexyl part of Lomustine with TEMPO radical did not suppress the BBB permeability of the drug. Both drugs (SLENU and TEMPOL) manifested a similar permeability. The data from diffusion-weighted MRI confirmed this assumption. SLENU was detected in the brain tissue (cortex, thalamus, hypothalamus), as well as in the brain ventricles. After free-water signal suppression by a diffusion-weighted MRI technique with motion probing gradients, the MRI signal remained in the tissue (data are not shown).

The MRI signal enhancement of nitroxyl radical disappeared quickly (within 2–3 min) after passing of SLENU from the blood vessels in the brain tissue. Presumably, this is due to the high permeability of SLENU for cell membranes, which is accompanied by rapid reduction of nitroxyl radical to the respective hydroxylamine in the brain cells and loss of MRI signal enhancement. In the surrounding tissues, the MRI signal had a better stability and a slightly longer half-life.

The fast detection of MRI signal enhancement could be considered as an advantage, because of the shortening of the time of the analytical and diagnostic process.

The present study is just a first trial for using nitroxyl radicals for spin-labelling of conventional drugs and non-invasive, dynamic MR imaging of their BBB permeability. We have tried to show the advisability of this concept. Novel synthetic strategies are necessary to improve the contrast and stability of nitroxyl label in the brain tissue without affecting its BBB permeability, which will allow higher spatial resolution of signal-to-noise ratio and will facilitate real-time MRI data reconstruction and quantitative analysis. The exchange of TEMPO radical with 2,2,5,5-tetramethyl-pyrrolidinyl-1-oxyl (PROXYL radical) is a promising strategy for increasing the contrast and stability of an MRI signal in the brain[17] and other tissues (Fig. 2S, *Supplementary Information*†).

It is necessary to note that nitroxyl radicals have low toxicity and are comparatively harmless to living organisms. TEMPOL—one of the most famous commercially available nitroxyls, is in phase I of clinical trials, as a preventer of alopecia in radiation-treated cancer patients.[23] The combined application of nitroxyls and conventional chemotherapeutics increases the anticancer effect and suppresses the multidrug resistance.[24] Therefore, the nitroxyl-labelling could be considered as environmentally friendly and with minimal risk for humans. There is one more advantage in nitroxyl-labelling and imaging. The dynamic of MRI signal enhancement gives additional information concerning the oxi-redox status of the brain tissue. This information could be useful for planning of conventional chemo- and radiotherapy of cancer and other diseases. The described approach is applicable not only for non-invasive imaging of BBB permeability for conventional drugs, but also for imaging of their localization in other organs and tissues, using MRI.

The technical support of Dr Antoaneta Zheleva (Trakia University, Bulgaria) and Ms Sayaka Shibata (NIRS-Chiba, Japan) is gratefully acknowledged.

## Notes and references

1 L. Zhang, H. Zhu, T. I. Oprea, A. Golbraikh and A. Tropsha, *Pharm. Res.*, 2008, **25**, 1902.
2 D. D. Shen, A. A. Artru and K. K. Adkison, *Adv. Drug Delivery Rev.*, 2004, **56**, 1825.
3 D. Pan, M. Iyer, J. Liu, Y. Li and A. J. Hopfinger, *J. Chem. Inf. Comput. Sci.*, 2004, **44**, 2083.
4 A. K. Dash and W. F. Elmquist, *J. Chromatogr., B: Anal. Technol. Biomed. Life Sci.*, 2003, **797**, 241.
5 M. Gumbleton and K. L. Audus, *J. Pharm. Sci.*, 2001, **90**, 1681.
6 D. M. Killian, L. Gharat and P. J. Chikhale, *Drug Delivery*, 2000, **7**, 21.
7 V. Josserand, H. Pélerin, B. de Bruin, B. Jego, B. Kuhnast, F. Hinnen, F. Ducongé, R. Boisgard, F. Beuvon, F. Chassoux, C. Daumas-Duport, E. Ezan, F. Dollé, A. Mabondzo and B. Tavitian, *J. Pharmacol. Exp. Ther.*, 2006, **316**, 79.
8 N. J. Abbott, D. C. Chugani, G. Zaharchuk, B. R. Rosen and E. H. Lo, *Adv. Drug Delivery Rev.*, 1999, **37**, 253.
9 R. Weissleder and U. Mahmood, *Radiology*, 2001, **219**, 316.
10 K. Takeshita and T. Ozawa, *J. Radiat. Res. (Tokyo)*, 2004, **45**, 373.
11 B. P. Soule, F. Hyodo, K. Matsumoto, N. L. Simone, J. A. Cook, M. C. Krishna and J. B. Mitchell, *Antioxid. Redox Signaling*, 2007, **9**, 1731.
12 L. Valgimigli, G. F. Pedulli and M. Paolini, *Free Radical Biol. Med.*, 2001, **31**, 708.
13 H. Utsumi and K. Yamada, *Arch. Biochem. Biophys.*, 2003, **416**, 1.
14 V. Afzal, R. C. Brasch, D. E. Nitecki and S. Wolff, *Invest. Radiol.*, 1984, **19**, 549.
15 K. Matsumoto, F. Hyodo, A. Matsumoto, A. P. Koretsky, A. L. Sowers, J. B. Mitchell and M. C. Krishna, *Clin. Cancer Res.*, 2006, **12**, 2455.
16 F. Hyodo, K. Matsumoto, A. Matsumoto, J. B. Mitchel and M. C. Krishna, *Cancer Res.*, 2006, **66**, 9921.
17 F. Hyodo, K.-H. Chuang, A. G. Goloshevsky, A. Sulima, G. L. Griffiths, J. B. Mitchell, A. P. Koretsky and M. C. Krishna, *J. Cereb. Blood Flow Metab.*, 2008, 1.
18 M. J. B. Taphoorn, M. J. Van den Bent, M. E. L. Mauer, C. Coens, J-Y. Delattre, A. A. Brandes, P. A. E. Smitt, H. J. J. A. Besrnsen, M. Frenay, C. C. Tijssen, D. Lacombe, A. Allgeier and A. Bottomley, *J. Clin. Oncol.*, 2007, **25**, 5723.
19 N. Bodor and P. Buchwald, *Adv. Drug Delivery Rev.*, 1999, **36**, 229.
20 V. Gadjeva and R. Koldamova, *Anti-Cancer Drug Des.*, 2001, **16**, 247.
21 A. M. Zheleva and V. G. Gadjeva, *Int. J. Pharm.*, 2001, **212**, 257.
22 V. Gadjeva, *Eur. J. Med. Chem.*, 2002, **37**, 295.
23 J. M. Metz, D. Smith, R. Mick, R. Lustig, J. Mitchell, M. Cherakuri, E. Glatstein and M. Hahn, *Clin. Cancer Res.*, 2004, **10**, 6411.
24 R. Ravizza, E. Cereda, E. Monti and M. B. Gariboldi, *Int. J. Oncol.*, 2004, **25**, 1817.

Gene Therapy (2009), 1–10

www.nature.com/gt

ORIGINAL ARTICLE

# Visualization of in vivo electroporation-mediated transgene expression in experimental tumors by optical and magnetic resonance imaging

W Aung[1,3], S Hasegawa[1,3], M Koshikawa-Yano[1], T Obata[2], H Ikehira[2], T Furukawa[1], I Aoki[2] and T Saga[1]

[1]Diagnostic Imaging Group, Molecular Imaging Center, National Institute of Radiological Sciences, Chiba, Japan and [2]Biophysics Group, Molecular Imaging Center, National Institute of Radiological Sciences, Chiba, Japan

In vivo *electroporation (EP) is an efficient method for effective gene transfer and is highly expected for application in anticancer gene therapy. Non-invasive monitoring of gene transfer/expression is critical for optimal gene therapy. Here we report* in vivo *optical and high-field magnetic resonance imaging (MRI) of EP-mediated transgene expression in a tumor model. Initially, we observed spatio-temporal change in* in vivo *EP-mediated transgene expression by optical imaging using red fluorescence protein (RFP) as a reporter gene. Next, we constructed a dual-reporter plasmid carrying a gene-encoding MRI reporter ferritin heavy chain and* RFP *gene to visualize the intratumoral transgene expression by dual modality. Cells transfected with this plasmid showed lower signal intensity on* in vitro $T_2$*-weighted cellular MRI and quantitatively increased the transverse relaxation rate ($1/T_2$) compared with control cells. After conducting* in vivo *EP in an experimental tumor, the plasmid-injected region showed both fluorescent emissions in optical imaging and detectably lowered signal on $T_2$-weighted MRI. The correlative immunohistological findings confirmed that both the reporter transgenes were co-expressed in this region. Thus, our strategy provides a platform for evaluating EP-mediated cancer gene therapy easily and safely without administering contrast agent or substrate.*
Gene Therapy advance online publication, 21 May 2009; doi:10.1038/gt.2009.55

**Keywords:** in vivo *electroporation; transgene expression;* in vivo *optical imaging; magnetic resonance imaging*

## Introduction

Gene therapy is a novel treatment approach still under development, with several trials to cure diseases, such as monogenetic disorder and malignant disease having been carried out.[1,2] There are various methods for gene delivery and, currently *in vivo* gene transfer is on the basis of two ways: viral delivery and non-viral delivery. The former, generally, is a relatively efficient means of introducing a therapeutic gene to target cells. However, the method has some disadvantages, as there exists the potential for immunogenicity, random insertion and its mutagenesis in the genome, uncontrollable chronic expression of the gene, risk of systemic spread, and the fact that the quality control of viral particles for *in vivo* administration is a laborious and expensive protocol.[3] In contrast, non-viral gene delivery is believed to be safer than viral delivery, and it has been shown that efficient and long-term expression could be expected.[4,5]

Correspondence: Dr S Hasegawa or Dr W Aung, Diagnostic Imaging Group, Molecular Imaging Center, National Institute of Radiological Sciences, Anagawa 4-9-1, Inage-ku, Chiba 263-8555, Japan.
E-mails: shase@nirs.go.jp or winn@nirs.go.jp
[3]These authors contributed equally to this work.
Received 30 September 2008; revised 6 January 2009; accepted 6 January 2009

*In vivo* electroporation (EP) is a method that has emerged to facilitate gene delivery of naked plasmid DNA *in vivo*.[6] It has been used in the laboratory for gene delivery to cells *in vitro* or *in vivo*, and is recently receiving much attention in cancer gene therapy as a clinically applicable method for enhancing gene delivery, based on it being carried out safely and easily with low cost.[7–9] In this method, plasmid DNA is injected into target tissue after which a series of electric pulses that induce temporary and reversible breakdown of cell membrane and pore formation is conducted to augment DNA transport into the cells. It has been applied to not only accessible surface tissue but also to deep tissues.[10] Since the first application of the *in vivo* delivery of chemotherapeutic agents to solid tumor, study of the delivery of plasmid DNA to cancer by EP has grown tremendously. Many earlier studies have shown that intratumoral gene delivery by *in vivo* EP strongly inhibits tumor growth and generates systemic immunity against tumor in experimental models.[11–15] Furthermore, a clinical trial for melanoma treatment using *in vivo* EP has been started.[6] Like other gene delivery methods, non-invasive monitoring of *in vivo* EP-mediated transgene expression of the introduced gene is a critical issue for optimizing the protocol and ensuring efficacy of the treatment. However, non-invasive methods of monitoring EP-mediated transgene expression *in vivo* are not yet well established.

An *in vivo* molecular imaging technique with reporter gene has been used for the non-invasive detection of gene expression, providing information regarding the location and duration of therapeutic gene expression and even quantification of the expression level.[16,17] Reporter gene imaging for different imaging modalities, such as optical, magnetic resonance imaging (MRI) and positron emission tomography have been developed, and the techniques and protocols are being refined rapidly. It has been suggested that *in vivo* reporter gene imaging would be effective for the non-invasive monitoring of gene expression in gene therapy.[18–21]

The aim of this work was to develop a simple, reliable and safe method to visualize transgene expression in tumors mediated by *in vivo* EP in preclinical tumor models for the design of more rational gene therapy. Here, we report *in vivo* optical imaging and 7-T MRI of intratumoral transgene expression mediated by *in vivo* EP, using the corresponding reporter genes *red fluorescence protein* (*RFP*) and *ferritin heavy chain* (*FHC*), respectively.

## Results and discussion

### In vivo *optical imaging of transgene expression in tumor mediated by* in vivo *electroporation*

We initially sought to determine whether *in vivo* EP enhanced gene delivery into experimental tumors. For this purpose, we constructed pRFP, a plasmid DNA encoding a red fluorescence protein (RFP), DsRed-Express, transcribed by a composite promoter that combines the cytomegalovirus (CMV) immediate early enhancer and a modified chicken β-actin (CAG) promoter.[22] CAG promoter is more efficient than the classical CMV promoter that is often silenced during the establishment of cell lines that stably express the desired transgene.[23] We used plate-and-fork-type electrodes for *in vivo* EP based on the fact that this type was reported to be more effective for gene transfer than needle-type and plate-and-plate-type electrodes.[24,25] We injected a naked form of the plasmid DNA directly into 293T subcutaneous tumors in nude mice and then conducted EP in a tumor on the right, but not on the left side. *In vivo* optical imaging showed that the efficiency of plasmid delivery into the tumor was clearly different. In the tumor subjected to *in vivo* EP, RFP expression was easily detected, whereas fluorescence emission was nearly absent in the tumor subjected to plasmid injection only (Figure 1a), suggesting that *in vivo* EP enhances gene delivery *in vivo*. We then investigated the temporal change in the level of gene expression mediated by *in vivo* EP in the tumor models using serial optical imaging. *In vivo* EP-mediated DsRed RFP expression was visualized even on day 1 (Figure 1b), gradually increased up to its maximal level on about day 6 and decreased thereafter. More longitudinal monitoring of DsRed RFP expression showed that localized gene expression could be observed for over 2 weeks (Figure 1c). In some cases, it was detectable for even longer than 3 weeks (data not shown). Quantified fluorescent intensities are shown in bar graphs in Figures 1b and c. This kinetic pattern of expression was similar to that observed by Pedron-Mazoyer *et al.*[26] when they carried out intradermal EP of 50 μg of DsRed plasmid. Bloquel *et al.*[27] also reported similar kinetics of transgene expression when they injected 60 μg of a plasmid encoding luciferase in the mouse knee joint. In *ex vivo* tumors of killed mice, RFP expression was noted at the plasmid injection site, and RFP-expressing cells scattered in a heterogeneous pattern were clearly evident on confocal fluorescence microscopy of tumor cryosections (Figure 1d). The percentage of cells expressing RFP was estimated to be ~9% in the area where the plasmid DNA was electroporated most efficiently. Taken together, these data confirm that localized trangene expression in tumor is achievable for 2–3 weeks by *in vivo* EP,[28] and provide the basis for a better understanding of the kinetics of transgene expression mediated by *in vivo* EP.

### *A plasmid DNA construct for dual-modality imaging and alterations in cellular iron metabolism by expression of* FHC *gene*

We next sought to visualize the reporter transgene expression mediated by *in vivo* EP by MRI because of its compatibility with clinical use, applicability to repeated use without radiation risk and high spatial resolution without depth limitation.[16] Recently, ferritin or *FHC* gene has been suggested to be a reliable reporter transgene for MRI with a marked effect on solvent MR relaxation rates.[29–31] FHC is an intracellular iron-binding protein that has various biological functions in cells.[32] Overexpression of *FHC* reporter gene in cells causes $T_2$ (transverse relaxation time) change in its expression site without the exogenous administration of contrast agents. It has been assumed that this is on the basis of the redistribution of intracellular iron and that FHC reporter activation transiently lowers the labile iron pool in cells and augments iron uptake, probably through transferrin receptor (TfR) upregulation to compensate for iron deficiency. We chose the *FHC* gene as MR reporter gene because of its favorable reproducibility and lesser toxicity than other reporters, and because contrast agents would not be needed.[29–31,33] We also chose the use of *in vivo* optical imaging to easily evaluate gene delivery and determine the location of transgene expression in tumors. Therefore, we constructed pFHC–RFP, a bicistronic mammalian expression vector carrying human FHC cDNA and a gene encoding DsRed-Express placed downstream of an internal ribosome entry site (IRES) of the encephalomyocarditis virus (Figure 2a). The IRES sequence allowed the coordinated expression of two reporter genes transcribed by a single CAG promoter, enabling us to check the FHC reporter expression in cells by red fluorescence. As control vector, we created pX-RFP, in which IRES linked-DsRed Express gene was conserved but *FHC* gene was inserted in reverse direction. The 293T cells were transfected with pFHC–RFP or pX-RFP using lipofection. Under fluorescence microscopy, both transfected cells emitted detectable red fluorescence, whereas no fluorescence was observed in the cells without transfection (Figure 2a). Western blot analysis showed that a low level of endogenous FHC protein was expressed in 293T cells and that FHC reporter protein was robustly translated in cells with pFHC–RFP, but hardly with pX-RFP (Figure 2a). We investigated the temporal change in RFP expression in pFHC–RFP-transfected cells (Figure 2b). RFP expression was first visualized at 12–24 h, gradually increased up to its maximal level at 96 h after transfection and decreased

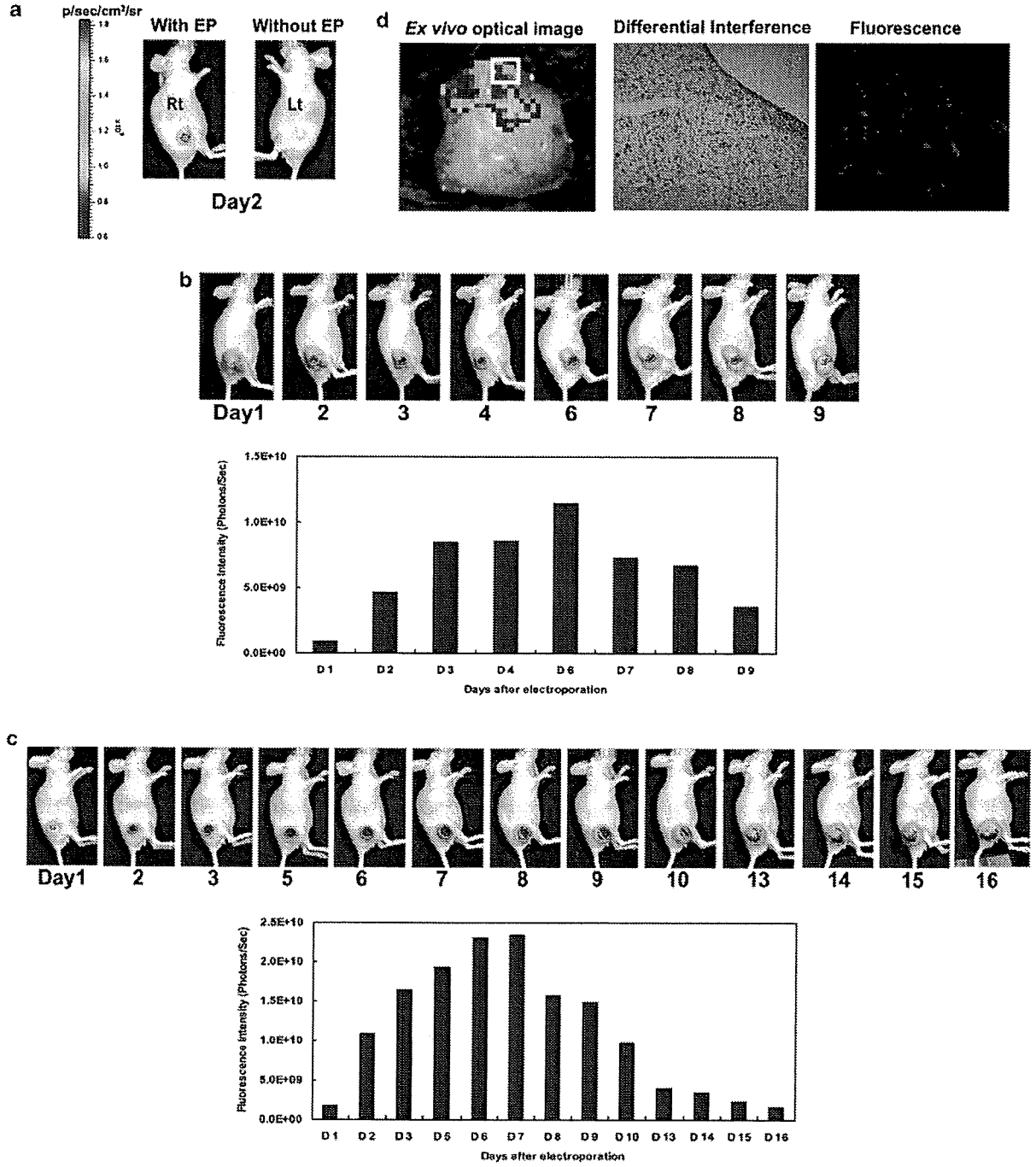


**Figure 1** Monitoring of electroporation (EP)-mediated transgene expression by *in vivo* optical imaging. (a) Comparison of transfection efficiency with and without *in vivo* EP in tumor models. Red fluorescence emission was detected in the tumor on the right side (Rt, with EP), whereas the tumor on the left side (Lt, without EP) showed only very faint light emission. (b) Representative images of tumor transfected with pRFP by *in vivo* EP. Days after EP are indicated under the images. Red fluorescence protein (RFP) expression was detected even on day 1, and gradually increased up to the maximal level on around day 6. Images were adjusted to the same scale. Columns, fluorescence intensities quantified in photons per sec. In the image of day 9, a red dotted line encircles the part of the tumor shown in panel d. (c) Representative images for longitudinal monitoring of localized, long-term RFP expression in a tumor followed for more than 2 weeks. Columns, fluorescence intensities detected on indicated days. Scale bar for images in panel b and c was shown in a. (d) *Ex vivo* optical imaging confirmed red fluorescence emission from the plasmid injection site in the tumor. The inset indicates the area shown in differential interference and fluorescence images of tumor cryosection (10 μm). Magnification, × 20. On confocal laser microscopy of tumor sections, red fluorescent cells were visualized as non-homogeneous scattered pattern.

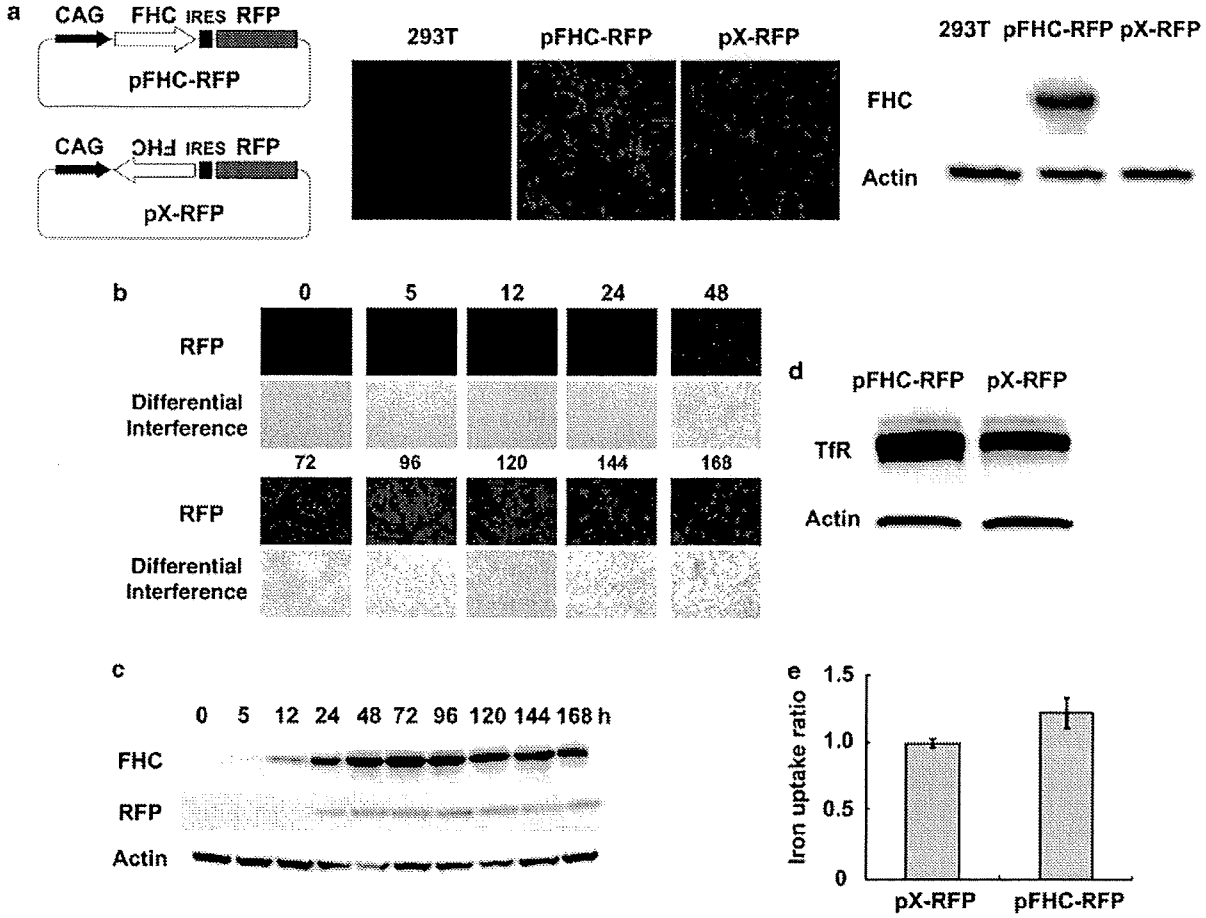


**Figure 2** Dual-reporter protein expression in 293T cells and alterations of cellular iron metabolism. (**a**) Expression of dual-reporter proteins in 293T cells. Schema of a plasmid DNA construct carrying dual-reporter genes (pFHC–red fluorescence protein (RFP)) and a control plasmid carrying *RFP* gene and reversely inserted ferritin heavy chain (*FHC*) gene (pX-RFP) is shown. Non-transfected 293T cells showed no fluorescence signal. Cells transfected with the vectors showed red fluorescence on fluorescence microscopic images. Moreover, robust expression of FHC reporter protein in cells transfected with pFHC–RFP vector was confirmed by western blotting. (**b**) RFP expression in the pFHC–RFP vector-transfected cells. RFP fluorescence and differential interference images are shown. Times (hour) after transfection are indicated above the images. (**c**) Time course study of FHC and RFP expression confirmed nearly correlated transcription in the transfected cells. Times (hour) for sampling are indicated above the image. Actin was used as loading control. (**d**) Upregulation of transferrin receptor (TfR) in cells transfected with pFHC–RFP vector was noted. Actin was used as loading control. (**e**) FHC over-expressing cells augmented iron uptake. Results were obtained from 24-h incubation with $^{59}$Fe. Radioactivity was counted from at least eight samples in two independent experiments and the counts were normalized by cell number. Mean ± s.d. IRES, internal ribosome entry site.

thereafter. The time course of FHC and RFP expression was examined in the pFHC–RFP-transfected cells using antibodies specific for each protein (Figure 2c). FHC expression appeared at 12 h, peaked at 72 h after transfection and slowly decreased. However, even 7 days (168 h) after transfection, FHC was still clearly detected. Consistent with the fluorescence microscopic images, RFP expression was first detected at 24 h and reached its maximum level at 96 h after transfection. Similar to FHC expression, RFP expression was also detectable at 7 days after transfection. It seemed that RFP was translated less efficiently than FHC, presumably because the expression of gene located downstream of IRES is often less efficient than that of its upstream gene.[34] Nevertheless, the RFP expression closely reflected the FHC expression, convincing us that monitoring the FHC expression would be sufficient. It has been reported that FHC overexpression induces TfR in the kidney of drug-inducible FHC transgenic mice.[35] We therefore evaluated TfR expression in cells with FHC reporter by western blotting. Consistent with the earlier result, TfR protein was increased in the cells with transient activation of FHC reporter compared with control cells (Figure 2d), suggesting that FHC reporter induces TfR upregulation. We then sought to determine whether FHC expression and its consequent upregulation of TfR altered the rate of iron influx in cells. It was found that iron uptake in cells with FHC reporter was increased by about 20% compared with reporter negative cells (Figure 2e). Taken together, these results suggest that our dual-reporter vector was functionally verified, and that activation of FHC reporter enhances iron uptake through TfR upregulation in cells.

### *Visualization of FHC reporter transgene expression by* in vitro *MRI*

We conducted MRI of cell pellets to investigate the effects of FHC on the MR signal. Cells were transfected with

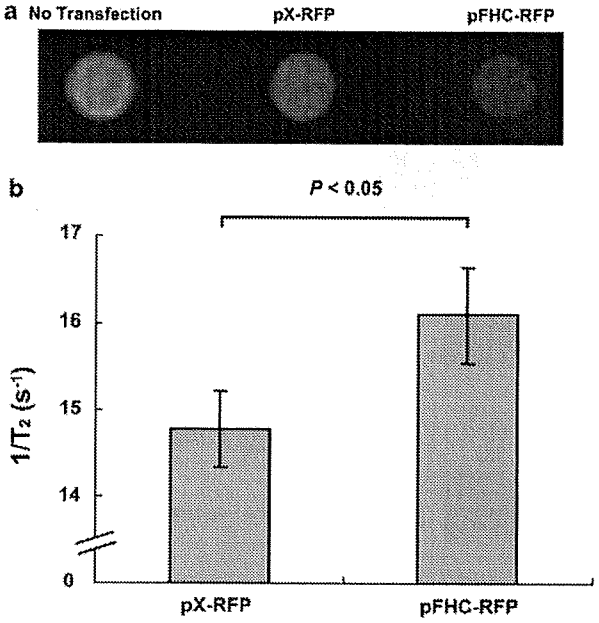


**Figure 3** Cellular magnetic resonance imaging. (a) A representative $T_2$-weighted magnetic resonance imaging of transfected and non-transfected cell pellets. TR/TE = 4000/75 ms. Cells transfected with pFHC–red fluorescence protein (RFP) showed lower signal intensity compared with cells with pX-RFP. (b) For quantitative analysis, the transverse relaxation rate ($1/T_2$) of cell pellets was compared between cells with pX-RFP and those with pFHC–RFP, suggesting significant $T_2$ shortening by FHC reporter expression ($P < 0.05$). Mean ± s.d. ($n = 3$).

pFHC–RFP or pX-RFP and incubated with standard cell medium supplemented with iron for 3 days before MRI. Consistent with the earlier results,[29,30] the pFHC–RFP-transfected cells showed lower signal intensity in $T_2$-weighted MRI compared with pX-RFP-transfected control cells (Figure 3a). Quantitative analysis showed that the transverse relaxation rate ($1/T_2$) of the cells transfected with pFHC–RFP was significantly higher than that of control cells (Figure 3b), confirming that FHC expression shortens $T_2$ as we predicted.

### In vivo *optical imaging and MRI of electroporation-mediated transgene expression in tumor*

To visualize the reporter transgene expression *in vivo* by optical imaging and MRI, we used 293T xenograft models and introduced naked pFHC–RFP or pRFP by *in vivo* EP. We carried out *in vivo* optical imaging and fluorescence stereoscopic microscopy before MRI. The information obtained from optical imaging ensured successful gene delivery and was helpful for the timing of MRI, enabling us to monitor the gene expression of FHC. Although RFP was expected to be less translated compared with FHC as mentioned above, we could readily detect RFP expression in tumor transfected with pFHC–RFP by both instrumentations (Figure 4a), and it was beneficial for choosing the MRI slices that covered the appropriate region where both reporters were expressed. In $T_2$-weighted MRI at 7 days after EP, tumors subjected to pRFP showed relatively homogeneous intensity, whereas tumors subjected to pFHC–RFP showed spotty but detectable hypo-intensity areas in the MRI slices (Figure 4b), showing that the ferritin MRI reporter system functions not only in a drug-inducible reporter system or highly efficient viral delivery system, but also in gene delivery with a relatively low transfection efficiency, such as *in vivo* EP. To validate the MRI results, the tumor was excised and carefully sectioned to obtain almost the same plane as seen on the MR image. RFP expression in the cross-section was observed correspondingly in the area showing low intensity in $T_2$WI (Figure 4c), suggesting that the $T_2$ change is attributable to the FHC reporter expression. For comparison of $T_2$-shortened areas in the tumors between RFP-tumor and FHC-tumor, we calculated mean $T_2$ in control RFP-tumors (57.6 ± 3.0 ms, see Materials and methods) and counted the number of pixels having a relaxation time below 51.6 ms (lower limit of two s.d. of mean $T_2$) in RFP-tumors and FHC tumors. This showed that the percentage of pixels showing $T_2$ shortening in FHC tumors was significantly increased compared with that in RFP-tumors (Figure 4d). These findings were consistent with the results of *in vitro* cellular MRI and strongly supported the notion that the hypo-intensity observed in *in vivo* $T_2$-weighted MRI resulted from FHC reporter expression.

### *Expression of both reporter proteins in FHC-transfected tumors*

After *ex vivo* tumors were carefully sectioned to obtain a plane corresponding to an MRI-oriented image, we conducted fluorescence microscopic analysis and immunohistochemistry using antibodies specific for ferritin protein. RFP expression was clearly detected, with little or weak staining of ferritin being observed in RFP-tumor. In contrast, cells strongly stained by the antibody were observed in FHC-tumor, and they were well correlated with RFP-positive cells (Figure 5), confirming the correlation between RFP and FHC reporter expression.

In conclusion, we showed the dual modality of *in vivo* optical imaging and MRI of EP-mediated reporter transgene expression in experimental tumors. The method allowed us to visualize gene expression in samples with a broad scale from macroscopic to microscopic levels by using even a kind of plasmid vector. It is superior to other methods in respect to not needing to administer contrast agents and substrates, repetitive use capability and imaging at high spatial resolution. Our MRI detection using FHC reporter would be a clinically appropriate method for evaluating gene therapy mediated by *in vivo* EP even in cases of repeated protocol. Given that optical imaging and MRI are complementary in terms of high temporal resolution and sensitivity of the former and high spatial resolution of the latter, and that fluorescence imaging is evolving toward clinical application,[36] their combination may provide a new opportunity for evaluation of *in vivo* gene delivery to various tissues ranging widely from body surface to deep tissues in future clinical scenarios. In the gene therapy setting, if one connects the reporter genes to a therapeutic gene, the location, magnitude and duration of therapeutic gene co-expression with the reporter genes can be monitored non-invasively. Cancer gene therapy using *in vivo* EP has shown to be effective

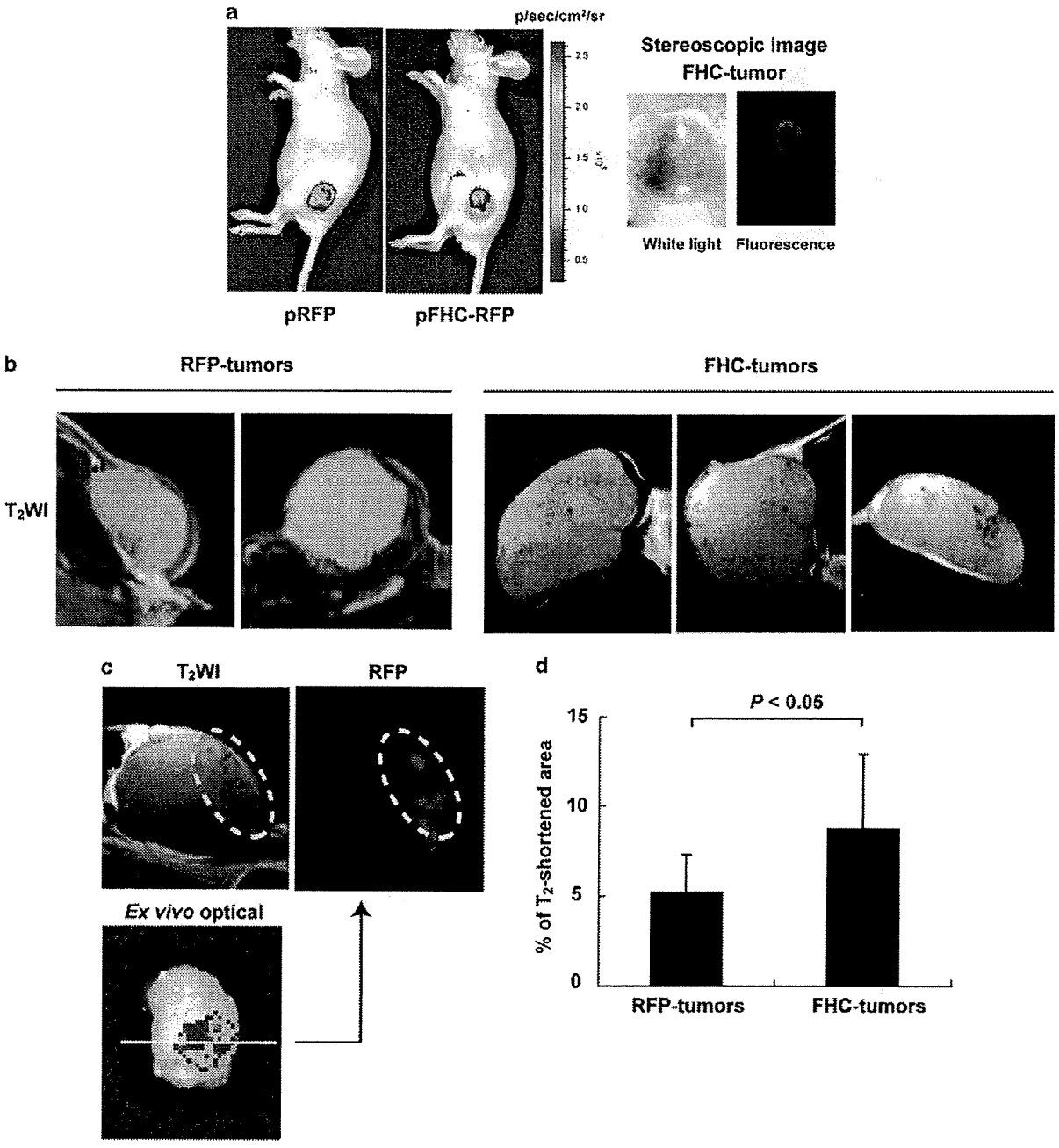


**Figure 4** *In vivo* optical imaging and magnetic resonance imaging (MRI) of electroporation-mediated transgene expression. (**a**) Representative *in vivo* optical images of tumors transfected with pRFP or pFHC–red fluorescence protein (RFP) are shown. Stereoscopic fluorescence images of tumor transfected with pFHC–RFP (ferritin heavy chain (FHC)-tumor) conferred to the *in vivo* optical image showed a consistent light emission area. (**b**) Representative MRI $T_2$-weighted images ($T_2$WI) of tumors transfected with pRFP (RFP-tumors) or pFHC–RFP (FHC-tumors). Spotty low signal intensity areas were present in part of the FHC-tumors, whereas relatively homogeneous intensity was noted in RFP-tumors. TR/TE = 3000/50–60 ms. (**c**) Correlation between low-signal area in $T_2$WI and RFP expression in an FHC-tumor. A representative $T_2$WI of FHC-tumor and RFP expression in a cross-section derived from the same tumor are shown. Corresponding regions are surrounded by yellow dotted line. As a reference, *ex vivo* optical imaging of the tumor was also shown. The cross-section was obtained by dissection of *ex vivo* tumor at the white line with the aid of stereoscopic microscopy. (**d**) Comparison of $T_2$-shortened area between FHC-tumors and RFP-tumors. The percentage of pixels below the lower threshold limit (−2 s.d. of mean $T_2$ of RFP-tumors) was significantly increased in FHC-tumors ($P < 0.05$). Mean+s.d. ($n = 4$ for RFP-tumors, $n = 6$ for FHC-tumors).

in preclinical animal models, giving support to our approach. Although improvements to resolve the limitations of each modality are still needed, the 'proof-of-concept' approach we show in this report would be beneficial to the design of more efficient *in vivo* EP-mediated cancer gene therapy.

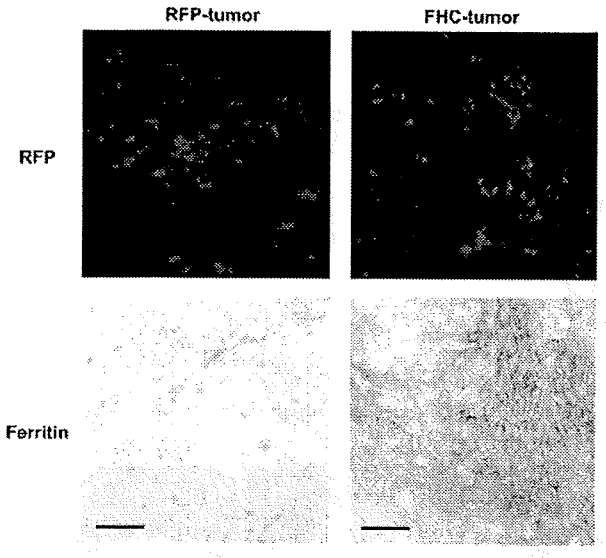


**Figure 5** Expression of reporter proteins in a tumor section. Red fluorescence protein (RFP) and ferritin expression in the cryosection (7 μm) of a RFP- and a ferritin heavy chain-tumor. RFP was detected by fluorescence microscope and ferritin protein was stained by mouse anti-human ferritin antibody. Magnification, ×20. Scale bars = 50 μm.

## Materials and methods

### *Cell lines*

Human embryonic kidney 293T cells were cultured in DMEM (Sigma-Aldrich, St Louis, MO, USA) with 10% fetal bovine serum, 100 U $ml^{-1}$ of penicillin and 100 μg $ml^{-1}$ of streptomycin.

### *Plasmid*

pRFP was constructed by insertion of DsRed-Express cDNA excised from pDsRed-Express (Clontech, Mountain View, CA, USA) into pCAGGS (kindly provided by Oriental Yeast Corp., Tokyo, Japan). For pFHC–RFP or pX-RFP, human FHC cDNA was cloned into a multiple cloning site of pIRES2-DsRed-Express (Clontech) at correct or reverse direction, respectively, and the resultant DNA fragment containing IRES and DsRed-Express was excised and ligated to pCAGGS.

### *Lipofection*

The 293T cells were transfected with the vectors described above by Lipofectamine 2000 (Invitrogen Corp., Carlsbad, CA, USA) according to the manufacturer's instructions.

### *Western blotting*

The procedures to detect FHC and RFP were described earlier.[32] In brief, cell lysates were separated on a 12.5% polyacrylamide gel and transferred to Immobilon-P membrane (MILLIPORE, Billerica, MA, USA). We used rabbit anti-human FHC antibody (Santa Cruz Biotechnology, Santa Cruz, CA, USA) or rabbit anti-DsRed antibody (Clontech) as a primary antibody for detection of FHC or RFP, respectively. In both cases, anti-rabbit IgG conjugated with horseradish peroxidase (GE Healthcare UK Ltd., Little Chalfont, UK) was used as a secondary antibody. For detection of TfR, total cell lysates were separated on a 7.5% polyacrylamide gel and transferred to Immobilon-P membrane. The blot was blocked by TBS BLOTTO A (Santa Cruz) at room temperature (RT) for 2 h and incubated with primary antibody at RT for 2 h. As a primary antibody, mouse anti-human TfR antibody (ZYMED, South San Francisco, CA, USA) was used at a concentration of 1 μg $ml^{-1}$. The membrane was washed three times with Tris-buffered saline containing 0.05% Tween 20, and incubated with an anti-mouse IgG conjugated with horseradish peroxidase (GE Healthcare). The blots were developed with ECL plus western blotting detection system (GE Healthcare). Images were obtained by Chemi-Smart 5000 (Vilber Lourmat, Marne-la-Vallée, France).

### *$^{59}Fe$ uptake assay*

The 293T cells were transfected with 1.6 μg of plasmid DNAs in a 12-well dish. One day after the transfection, $^{59}FeCl_3$ (Perkin Elmer, Boston, MA, USA) was added to the wells and incubated for 24 h. Cells were washed three times in phosphate-buffererd saline and radioactivity was measured by gamma counter (ALOKA, Tokyo, Japan). The counts were normalized by cell number.

### *Animal tumor model*

The tumor xenograft model was developed by subcutaneous injection of $1 \times 10^7$ of 293T cells in 200 μl of Hanks' balanced salt solution (Invitrogen) in the lower back of nude mice (8–10-week-old female BALB/cA Jcl-nu/nu mice; CLEA, Tokyo, Japan). Tumor-bearing mice were subjected to *in vivo* EP when the tumor had reached an appropriate volume, mostly 75–150 $mm^3$ (usually 2 or 3 weeks after implantation). All animal model experiments were carried out in accordance with the guidelines for animal experimentation of the National Institute of Radiological Sciences.

### In vivo *electroporation*

*In vivo* EP was carried out when tumors reached diameters of more than 5 mm. For all *in vivo* EP, we used a plate-and-fork-type electrode CUY663-5X8 (NEPA GENE, Ichikawa, Japan) and CUY21SC electoroporator (NEPA GENE) with constant electrical parameters. Detailed analysis of *in vivo* EP was described by Takei *et al*.[25] After anesthetizing the mouse, the fork-arm of the electrode was inserted into the undersurface of the tumor, the tumor was pinched by both arms and electrical resistance was measured and adjusted to below 1 KΩ, ideally 0.8–0.5 KΩ. Then, the plasmid DNA in phosphate-buffererd saline (80 μg/40 μl) was injected directly into the tumor by a 30-gauge needle, and EP was immediately carried out. Five electrical pulses were delivered with pulse length of 50 ms and 50 V field strength. In the second cycle, another five pulses with opposite polarity were administered. To reduce the electrical resistance of skin, the plate-arm surface was covered with an electrocardiogram pad.

### In vivo *optical imaging*

Fluorescence light emission from tumors was monitored by IVIS lumina optical imaging system (Xenogen Corp., Alameda, CA, USA). Mice bearing xenograft tumors

were anesthetized by inhalation of 2.5% isoflurane and placed in a light-tight chamber. We selected the filter set for DsRed (excitation: 500–550 nm, emission: 575–650 nm, blue-shifted background excitation: 460–490 nm) and set the constant imaging parameters (exposure time: 2 s, binning: medium, lens aperture (f/stop): 2, field of view: 12.5 cm, floor lamp level: high). To obtain the autofluorescent-corrected image, the background filter image was subtracted from the primary excitation filter image using the Image Math tool and appropriate scale factor, according to the Living Image software version 2.6 (Xenogen Corp.) manual. The fluorescent area in the tumor, the region of interest, was encircled by hand, and the emission of light was quantified as photons per second. Then, the fluorescent area of *in vivo* tumor was re-confirmed by fluorescence stereoscopic microscope MZ16F (Leica Microsystem, Wetzlar, Germany).

### Ex vivo *optical imaging*

Mice were killed and tumors were excised and stripped skin out. Optical images of *ex vivo* tumors were acquired using the IVIS imaging system with the same settings as described above in *in vivo* optical imaging, and also by fluorescence stereoscopic microscope MZ16F.

### *Fluorescence microscopy*

Fluorescence from transfected cells or frozen sections of tumors was observed by Olympus FV1000 confocal laser microscopy system (Olympus, Tokyo, Japan), using a 543-nm excitation line and high-performance sputtered filter for DsRed or Olympus BX50 fluorescence microscope.

### In vitro *MRI measurement*

The 293T cells were transfected with 8 μg of plasmid DNAs in a 60-mm dish. Cell medium was removed the next day, and 200 μM of ferric ammonium citrate in the standard medium was added every 24 h. After 72-h incubation with the iron supplementation, cells were washed, harvested, transferred to a 96-well PCR plate (INA OPTIKA, Osaka, Japan) and centrifuged. The 96-well PCR plate was cut to 6 × 6 matrix tubes and set on a cradle (made in-house) for stable and homogeneous MRI measurement. Proton MRI was carried out in a 7.0-T, 40-cm bore magnet (Jastec and Kobelco, Kobe, Japan) with 11.6-cm inner-diameter field gradient system (BGA-12, Bruker Biospin, Ettlingen, Germany) interfaced to a Bruker Avance console (Bruker). A 70-mm-diameter birdcage radio frequency coil (Bruker) for both transmitting and receiving was used. Multi-echo images were acquired 2 h after cell preparation using a spin-echo pulse sequence with pulse repetition time (TR) = 4000 ms, number of echoes = 16 (15–240, 15 ms increment), matrix = 128 × 128, FOV = 40 × 40 mm, slice thickness = 1 mm and in-plane resolution = 312.5 μm. We regarded the multi-echo images obtained by TE = 50–80 ms as $T_2$-weighted images. Slice orientation was horizontal, and it was adjusted to the cell pellets in the PCR tubes. Sample temperature was maintained at room temperature (~23 °C). Quantitative $T_2$ maps were calculated by a non-linear least-squares fitting using MRvision software (MRVision Co., Winchester, MA, USA) on Linux PC (Red Hat Linux, Mountain View, CA, USA). Region of interests were defined as precipitated cell regions. Mean ± s.d. of three independent samplings was used for statistical analysis.

### In vivo *MRI measurement*

Mice bearing xenograft tumors were subjected to *in vivo* EP with pFHC–RFP or pRFP; gene expression was confirmed by optical imaging at 7 days after EP, and then MRI was conducted. The mice were anesthetized with 2.0% isoflurane, placed in a left or right lateral position and anesthesia was maintained at this level. During the experiment, a flow of warm air over the animal maintained body temperature at ~37.0 °C. Respiratory rate, monitored throughout the experiment, was maintained at 20–40 breaths per minute. *In vivo* MRI was acquired using the same 7.0-T magnet and field gradient system. The 70-mm-diameter birdcage radio frequency coil (Bruker) for transmitting and a saddle-shaped 2-channel phased array receiving surface coil (Rapid Biomedical, Rimper, Germany) were used. Multi-echo images were acquired using a spin-echo pulse sequence with TR = 3000 ms, number of echoes = 12 (10–120, 10 ms increments), matrix 256 × 256, FOV = 32 × 32 mm, slice thickness = 1 mm, in-plane resolution = 125 μm and slice gap = 1.2–1.8 mm. Slice orientation was transverse, and was localized in the tumor. Two adjacent transverse slices covering the area of RFP expression seen on the *in vivo* optical image were selected for generating quantitative $T_2$ maps. For tissue analysis on the $T_2$ maps, mean and s.d. of $T_2$ in the tumor was calculated out from all slices of RFP-transfected tumors. Then, the '$T_2$-shortened area' was defined as pixels that were below the threshold level as −2 s.d. of the mean $T_2$. Percentages of the '$T_2$-shortened area' of the entire tumor area in the plane were calculated and compared between the RFP-transfected and FHC-transfected tumor.

### *Immunohistochemistry*

Tumors subjected to EP were excised after MRI and the orientation of the transfected areas was re-checked with the aid of fluorescence stereoscopic microscopy. The tumor specimens were embedded in OCT compound and sectioned in the same direction as MRI into 7-μm thick slices. Cryosections were fixed in 4% paraformaldehyde phosphate buffer solution (Wako, Osaka, Japan). Immunohistochemistry was done using the Vector M.O.M peroxidase immunodetection kit and ImmPACT DAB substrate (Vector Laboratories, Burlingame, CA, USA) in accordance with the manufacturer's instructions. We used a mouse monoclonal antibody against human ferritin (0.5 μg $ml^{-1}$, BMA Biomedicals, Augst, Switzerland) as primary antibody.

### *Statistical analysis*

Significance of differences was determined by Student's *t*-test. *P*-values $<0.05$ were considered significant.

## Conflict of interest

The authors declare no conflicts of interest.

## Acknowledgements

We thank Dr Paolo Arosio (University of Brescia, Italy) for the generous gift of ferritin cDNA; Dr Jun-ichi Miyazaki (Osaka University, Japan) for the generous donation of pCAGGS vector; Kosho Suzuki (NEPA GENE) for technical suggestions for *in vivo* EP; Michiko Narazaki, Misao Yoneyama, Sayaka Shibata and Shigeyoshi Saito for skillful assistance with the MRI experiments; Hikaru Takenaka for preparation of the paper; members in our group for helpful discussions; Drs Yasuhito Sasaki, Yoshiharu Yonekura and Shuji Tanada for encouragements for this study. This study was supported in part by a Grant-in-Aid for Scientific Research for Exploratory Research from the Ministry of Education, Culture, Sports, Science and Technology, Japan (18659357: S Hasegawa); Intramural Research Grant from the National Institute of Radiological Sciences (S Hasegawa).

## References

1 Alexander BL, Ali RR, Alton EW, Bainbridge JW, Braun S, Cheng SH *et al.* Progress and prospects: gene therapy clinical trials (part 1). *Gene Therapy* 2007; **14**: 1439–1447.
2 Aiuti A, Bachoud-Levi AC, Blesch A, Brenner MK, Cattaneo F, Chiocca EA *et al.* Progress and prospects: gene therapy clinical trials (part 2). *Gene Therapy* 2007; **14**: 1555–1563.
3 Porteus MH, Connelly JP, Pruett SM. A look to future directions in gene therapy research for monogenic diseases. *PLoS Genet* 2006; **2**: e133.
4 Payen E, Bettan M, Rouyer-Fessard P, Beuzard Y, Scherman D. Improvement of mouse beta-thalassemia by electrotransfer of erythropoietin cDNA. *Exp Hematol* 2001; **29**: 295–300.
5 Argyros O, Wong SP, Niceta M, Waddington SN, Howe SJ, Coutelle C *et al.* Persistent episomal transgene expression in liver following delivery of a scaffold/matrix attachment region containing non-viral vector. *Gene Therapy* 2008; **15**: 1593–1605.
6 Daud AI, DeConti RC, Andrews S, Urbas P, Riker AI, Sondak VK *et al.* Phase I trial of interleukin-12 plasmid electroporation in patients with metastatic melanoma. *J Clin Oncol* 2008; **26**: 5896–5903.
7 Shimao K, Takayama T, Enomoto K, Saito T, Nagai S, Miyazaki J *et al.* Cancer gene therapy using *in vivo* electroporation of Flt3-ligand. *Int J Oncol* 2005; **27**: 457–463.
8 Kaiga T, Sato M, Kaneda H, Iwakura Y, Takayama T, Tahara H. Systemic administration of IL-23 induces potent antitumor immunity primarily mediated through Th1-type response in association with the endogenously expressed IL-12. *J Immunol* 2007; **178**: 7571–7580.
9 Golzio M, Mazzolini L, Ledoux A, Paganin A, Izard M, Hellaudais L *et al. In vivo* gene silencing in solid tumors by targeted electrically mediated siRNA delivery. *Gene Therapy* 2007; **14**: 752–759.
10 Isaka Y, Imai E. Electroporation-mediated gene therapy. *Expert Opin Drug Deliv* 2007; **4**: 561–571.
11 Goto T, Nishi T, Tamura T, Dev SB, Takeshima H, Kochi M *et al.* Highly efficient electro-gene therapy of solid tumor by using an expression plasmid for the herpes simplex virus thymidine kinase gene. *Proc Natl Acad Sci USA* 2000; **97**: 354–359.
12 Lohr F, Lo DY, Zaharoff DA, Hu K, Zhang X, Li Y *et al.* Effective tumor therapy with plasmid-encoded cytokines combined with *in vivo* electroporation. *Cancer Res* 2001; **61**: 3281–3284.
13 Tamura T, Nishi T, Goto T, Takeshima H, Dev SB, Ushio Y *et al.* Intratumoral delivery of interleukin 12 expression plasmids with *in vivo* electroporation is effective for colon and renal cancer. *Hum Gene Therapy* 2001; **12**: 1265–1276.
14 Lucas ML, Heller L, Coppola D, Heller R. IL-12 plasmid delivery by *in vivo* electroporation for the successful treatment of established subcutaneous B16.F10 melanoma. *Mol Ther* 2002; **5**: 668–675.
15 Matsubara H, Mizutani Y, Hongo F, Nakanishi H, Kimura Y, Ushijima S *et al.* Gene therapy with TRAIL against renal cell carcinoma. *Mol Cancer Ther* 2006; **5**: 2165–2171.
16 Massoud TF, Gambhir SS. Molecular imaging in living subjects: seeing fundamental biological processes in a new light. *Genes Dev* 2003; **17**: 545–580.
17 Golzio M, Rols MP, Gabriel B, Teissie J. Optical imaging of *in vivo* gene expression: a critical assessment of the methodology and associated technologies. *Gene Ther* 2004; **11**(Suppl 1): S85–S91.
18 Inubushi M, Wu JC, Gambhir SS, Sundaresan G, Satyamurthy N, Namavari M *et al.* Positron-emission tomography reporter gene expression imaging in rat myocardium. *Circulation* 2003; **107**: 326–332.
19 Serganova I, Blasberg R. Reporter gene imaging: potential impact on therapy. *Nucl Med Biol* 2005; **32**: 763–780.
20 Furukawa T, Lohith TG, Takamatsu S, Mori T, Tanaka T, Fujibayashi Y. Potential of the FES-hERL PET reporter gene system—basic evaluation for gene therapy monitoring. *Nucl Med Biol* 2006; **33**: 145–151.
21 Siddiqui F, Barton KN, Stricker HJ, Steyn PF, Larue SM, Karvelis KC *et al.* Design considerations for incorporating sodium iodide symporter reporter gene imaging into prostate cancer gene therapy trials. *Hum Gene Ther* 2007; **18**: 312–322.
22 Niwa H, Yamamura K, Miyazaki J. Efficient selection for high-expression transfectants with a novel eukaryotic vector. *Gene* 1991; **108**: 193–199.
23 Brooks AR, Harkins RN, Wang P, Qian HS, Liu P, Rubanyi GM. Transcriptional silencing is associated with extensive methylation of the CMV promoter following adenoviral gene delivery to muscle. *J Gene Med* 2004; **6**: 395–404.
24 Maruyama H, Ataka K, Higuchi N, Sakamoto F, Gejyo F, Miyazaki J. Skin-targeted gene transfer using *in vivo* electroporation. *Gene Therapy* 2001; **8**: 1808–1812.
25 Takei Y, Nemoto T, Mu P, Fujishima T, Ishimoto T, Hayakawa Y *et al. In vivo* silencing of a molecular target by short interfering RNA electroporation: tumor vascularization correlates to delivery efficiency. *Mol Cancer Ther* 2008; **7**: 211–221.
26 Pedron-Mazoyer S, Plouet J, Hellaudais L, Teissie J, Golzio M. New anti angiogenesis developments through electro-immunization: optimization by *in vivo* optical imaging of intradermal electro gene transfer. *Biochim Biophys Acta* 2007; **1770**: 137–142.
27 Bloquel C, Trollet C, Pradines E, Seguin J, Scherman D, Bureau MF. Optical imaging of luminescence for *in vivo* quantification of gene electrotransfer in mouse muscle and knee. *BMC Biotechnol* 2006; **6**: 16.
28 Heller LC, Ugen K, Heller R. Electroporation for targeted gene transfer. *Expert Opin Drug Deliv* 2005; **2**: 255–268.
29 Genove G, DeMarco U, Xu H, Goins WF, Ahrens ET. A new transgene reporter for *in vivo* magnetic resonance imaging. *Nat Med* 2005; **11**: 450–454.
30 Cohen B, Dafni H, Meir G, Harmelin A, Neeman M. Ferritin as an endogenous MRI reporter for noninvasive imaging of gene expression in C6 glioma tumors. *Neoplasia* 2005; **7**: 109–117.
31 Cohen B, Ziv K, Plaks V, Israely T, Kalchenko V, Harmelin A *et al.* MRI detection of transcriptional regulation of gene expression in transgenic mice. *Nat Med* 2007; **13**: 498–503.

32 Aung W, Hasegawa S, Furukawa T, Saga T. Potential role of ferritin heavy chain in oxidative stress and apoptosis in human mesothelial and mesothelioma cells: implications for asbestos-induced oncogenesis. *Carcinogenesis* 2007; **28**: 2047–2052.
33 Gilad AA, Winnard Jr PT, van Zijl PC, Bulte JW. Developing MR reporter genes: promises and pitfalls. *NMR Biomed* 2007; **20**: 275–290.
34 Ngoi SM, Chien AC, Lee CG. Exploiting internal ribosome entry sites in gene therapy vector design. *Curr Gene Ther* 2004; **4**: 15–31.
35 Wilkinson JT, Di X, Schonig K, Buss JL, Kock ND, Cline JM *et al*. Tissue-specific expression of ferritin H regulates cellular iron homoeostasis *in vivo*. *Biochem J* 2006; **395**: 501–507.
36 Weissleder R, Pittet MJ. Imaging in the era of molecular oncology. *Nature* 2008; **452**: 580–589.

THE JOURNAL OF GENE MEDICINE
*J Gene Med* 2008; 10: 597–609.
Published online 28 March 2008 in Wiley InterScience (www.interscience.wiley.com) DOI: 10.1002/jgm.1164

RESEARCH ARTICLE

# Selective gene transfer into neurons via Na,K-ATPase β1. Targeting gene transfer with monoclonal antibody and adenovirus vector

Keiji Ishii[1,2]
Kiminori Nakamura[1]
Satoshi Kawaguchi[2]
Rong Li[1]
Sachie Hirai[1]
Naoya Sakuragi[1]
Takuro Wada[2]
Kazunori Kato[1]
Toshihiko Yamashita[2]
Hirofumi Hamada[1]*

[1]*Department of Molecular Medicine, Sapporo Medical University School of Medicine, Sapporo, Japan*

[2]*Department of Orthopedics, Sapporo Medical University School of Medicine, Sapporo, Japan*

*Correspondence to:
Hirofumi Hamada, Department of Molecular Medicine, Sapporo Medical University, South-1, West-17, Chuo-ku, Sapporo 060-8556, Japan.
E-mail: hhamada@sapmed.ac.jp

*Received: 28 February 2007*
*Revised: 4 December 2007*
*Accepted: 5 December 2007*



## Abstract

**Background** Neuron-selective gene transfer is an attractive therapeutic strategy for neurological disorders. However, optimal targets and gene delivery systems remain to be determined.

**Methods** Following immunization of mice with PC12 cells, hybridomas were screened by β-Gal reporter gene assay using FZ33 fiber-modified adenovirus vectors. Subsequently, the efficacy and specificity of monoclonal antibody (mAb)-mediated gene transfer via FZ33 and FdZ adenovirus vectors were evaluated by flow cytometry, chemiluminescent β-Gal reporter gene assay, and immunocytochemistry. Finally, the antigen recognized by the mAb was identified by mass spectrometry and transfection analysis.

**Results** A hybridoma clone 6E3 producing monoclonal antibody, mAb6E3, was screened. Flow cytometry, chemiluminescent β-Gal reporter gene assay, and immunocytochemistry with mAb6E3 and the fiber mutant adenovirus demonstrated efficient gene transfer into the PC12 cells. Treatment of neuron–glia cocultures with mAb6E3 and FdZ adenovirus resulted in neuron-selective gene transfer. Immunohistochemical images of rat spinal cord tissue showed that mAb6E3 reacts specifically with neurons. Finally, Na,K-ATPase β1 was identified as the antigen of mAb6E3.

**Conclusions** Hybridoma screening using FZ33 fiber-modified adenovirus vectors serves as an efficient approach to detect antigens in mAb-targeted gene transfer. Neuronal tropism in the central nervous system through mAb6E3 represents an important initial step towards neuron-selective gene transfer in the treatment of local neurological disorders, such as spinal cord injury. Copyright © 2008 John Wiley & Sons, Ltd.

**Keywords** adenovirus vector; gene therapy; Na,K-ATPase β1; neuron; targeting

## Introduction

Neurological disorders that result in severe physical loss of function and sensory disturbance remain intractable [1]. Gene therapy serves as a new treatment modality that potentially improves the prognosis of patients with neurological disorders [2–7]. One of the current challenges concerning gene therapy is the delivery of adequate genes into the appropriate cells. Without developing selective gene delivery systems, high efficacy of gene transfer by virus vectors may unintentionally lead to systemic and local adverse